Summer 8-20-2021

Structural and Material Characterization of Inflatable Drop-Stitch Panels Used in Bending Applications

Elisabeth M. Waugh
elisabeth.waugh@maine.edu

STRUCTURAL AND MATERIAL CHARACTERIZATION OF INFLATABLE DROP-STITCH PANELS USED IN BENDING APPLICATIONS

By

Elisabeth M. Waugh

B.S. University of Maine, 2018

A THESIS

Submitted in Partial Fulfillment of the

Requirements for the Degree of

Master of Science

(in Mechanical Engineering)

The Graduate School

The University of Maine

August 2021

Advisory Committee:

Senthil Vel, Professor Mechanical Engineering, Co-Advisor

William G. Davids, Professor of Civil and Environmental Engineering, Co-Advisor

Zhihe Jin, Professor of Mechanical Engineering

STRUCTURAL AND MATERIAL CHARACTERIZATION OF INFLATABLE DROP-STITCH PANELS USED IN BENDING APPLICATIONS

By Elisabeth M. Waugh

Thesis Advisors: Dr. Senthil Vel and Dr. William G. Davids, P.E.

An Abstract of the Thesis Presented
in Partial Fulfillment of the Requirements of the
Degree of Mater of Science
(in Mechanical Engineering)
August 2021

Inflatable beams, arches and panels have become increasingly popular for load-bearing applications and have a variety of military and civil applications. The popularity of these structures comes from being lightweight, easy to transport, and being able to regain shape after the structure has been overloaded and the load is removed. The majority of inflatable beams and arches – commonly termed "airbeams" – are cylindrical pressure vessels with a circular cross-section. In contrast, drop-stitch panels incorporate yarns that connect the top and bottom surfaces, giving a wide, shallow cross-section with parallel top and bottom surfaces. Unlike airbeams, drop-stich panels do not incorporate a bladder due to the presence of drop-yarns. Therefore, the majority of drop-stich panels use a coated fabric.

The primary objective of this research was to develop testing procedures to determine the constitutive properties of orthotropic neoprene/nylon drop-stitch inflatable panel fabric, and to quantify panel bending load-deflection response. This was done through panel inflation and skin coupon testing, large-scale torsion tests, and full-scale four-point bend tests. Panel inflation and skin coupon testing was done to determine the

effective panel orthotropic constitutive properties in the longitudinal/warp and transverse/weft directions of the panel. Torsion testing was performed to determine the membrane shear modulus. Full-scale panel bending tests to large displacements were used to quantify panel bending load-deflection response and the effect of inflation pressure on panel stiffness and capacity. The large-scale bend test load-deflection behavior was compared to the response estimated using the experimentally-determined skin constitutive properties. The bend test results indicated that there were likely significant shear deformations in the panel during bending, which was supported by the fact that the membrane shear modulus determined from the torsion tests was a small fraction of the membrane elastic moduli. While the actual response of the panel was softer than predicted using Euler beam theory, significantly stiffer response and higher capacities were observed at higher pressures as expected. It was also observed that with an increase in pressure, there is an increase in the membrane modulus. Prior literature has observed that the pressure-volume work effectively increases the shear rigidity (Davids and Zhang, 2008) (Davids, 2009). The increase in shear modulus with inflation pressure also contributes to the increase in panel bending stiffness.

DEDICATION

To my grandfather Waldamar Waugh,

I studied hard and learned a lot.

ACKNOWLEDGEMENTS

I would like to take a moment to acknowledge the key individuals that made my studies a pleasurable and productive experience here at the University of Maine. First and foremost I would like to thank my advisors Senthil Vel and William Davids for their guidance and patience over the last two years.

I would also like to thank Navatek LLC (now Martin Defense Group) for funding this drop-stitch inflatable research that I have been lucky to be a part of as a graduate student. Without funding, I may not have had the opportunity to work with Senthil Vel and Bill Davids.

I would also like to thank all my professors and the staff members at the ASCC for their continued support and knowledge that I will carry with me for the rest of my life. It has been a pleasure to work for and with all of them. Some individuals I would like to specifically acknowledge are John Arimond who offered me my first position as an undergraduate and extended an offer for this assistantship. Shawn Eary, Shawn Sewall and Tom Snape thank you for your guidance, support and endless source of entertainment. Ken Williams, I would not have had any working instrumentation if it were not for you. As well as Samuel Heathcote, who put up with my constant questions about ARAMIS and GOM.

A special thank you to Amanda Paradis. Without her countless hours of work and constant support for whatever needed to be done, I would have never been able to complete my research. She was a dedicated and motivated worker and her effort and friendship are greatly appreciated.

Throughout my many years at the University of Maine I have met many amazing and excellent friends. To name a few, Jacky McCarthy, Penny Allard, Jennifer Austin and Anne-Marie Engelsen your friendships are invaluable and I would like to thank you all for support, I would not have made it through graduate school without you all.

Finally, I would like to thank my family for their support through this entire process.

TABLE OF CONTENTS

LIST OF TABLES

LIST OF FIGURES

CHAPTER 1

INTRODUCTION

1.1 Prior Research on Inflatable Structures

Inflatable structures have become increasingly popular and have applications in a variety of industries, ranging from military to civilian use. The popularity of these structures comes from being lightweight, easy to transport, and their ability to regain shape after the structure has been overloaded and the load is removed. These structures have been used in applications for airships (Cavallaro, 2006), military tents (Brayley, 2011), boat hulls (Bagnell, 2011), stand up paddleboards (DiGiovanna, 2013), and protective crew quarters systems (Cavallaro and Smith, 2015) to name a few. Inflatable arches or airbeams are used for military tents, boat hulls and stand up paddleboards utilize drop-stitch panels, while protective crew quarters systems utilize both. Prior research mainly focused on the analysis of inflatable structures with a circular cross-section and experimental analysis to develop modelling.

Cavallaro et al. (2003) experimentally tested and analytically investigated the bending response of woven pressure-stabilized beams with a circular cross-section. The focus of the study was to observe the micro- and macro-mechanical properties of these pressurized structures. Cavallaro's work with air beams continued to characterize the constitutive properties of the fabric using biaxial tension and shear tests. These experimental values were used in finite element models to predict the bending behavior of air beams while accounting for air compressibility (Cavallaro et al., 2006). Suhey et al. (2005) conducted numerical modeling and design of inflatable structures with a circular cross-section for the application of open-ocean-aquaculture cages. It is important to note

that Suhey et al. (2005) assumed the material is anisotropic. Davids and Zhang (2008) developed a Timoshenko beam for a nonlinear analysis of inflatable arches. The finite element model accurately predicted the load-deflection response of pressurized, coated fabric beams in four-point bending by taking into consideration the effect of fabric wrinkling and the work done by pressure under deformation induced volume changes. Davids (2009) then expanded this modeling to include large deflections and a geometrically nonlinear analysis of pressurized fabric arches. Apedo et al. (2009) proposed a 3D Timoshenko's beam with a homogenous orthotropic fabric. The developed model proved that the loads depend on the mechanical properties as well as the inflation pressure, beam dimensions and the boundary conditions. Apedo et al. (2010) continued the study of inflatable orthotropic woven fabrics to develop linear and nonlinear finite element models. A cantilevered inflatable beam under a concentrated load was considered in their study. Kabche et al. (2011) studied the effect of inflation pressure on the constitutive properties of orthotropic woven fabrics when they are coated. An analytical approach to estimating the critical load of a homogenous orthotropic woven fabric was studied in Nguyen et al. (2011). This study was later continued by Nguyen et al. (2014) focusing on the inflation of a membrane tube. With the majority of literature exploring or presenting results on woven fabrics, Brayley (2011) and Brayley et al. (2012) focused on inflatable braided beams and arches with external reinforcing straps. These studies showed that there are creep effects in inflatable beams and external straps have an effect on pre-wrinkling response of the member. In a later study, braided beams were studied to be used as tubes in a torus for the United States National Aeronautics and Space Administration (NASA) (Clapp et al., 2015). In a subsequent study, Young et al. (2017) conducted full scale structural testing on the

inflatable torus members to be used for the Hypersonic Inflatable Aerodynamic Decelerator (HIAD). Elsabbagh (2015) developed a finite element model for an inflatable structure with a circular cross-section that has a radius that varies along the axial position of the beam.

All of the previous referenced literature specifically focuses on inflatable structures with a circular cross-section. While there is relatively little literature on the behavior of drop-stitch inflatable panels, they are still of increasing interest. When pressurized, inflatable structures balloon and take a circular shape, whereas drop-stitch panels incorporate yarns that drop down connecting the top and bottom membranes as seen in Figure 1.1 below. With sufficient drop-yarns, a flat surface can be achieved. Unlike airbeams and arches, drop-stich panels do not incorporate a bladder due to the presence of drop-yarns. Therefore, the majority of drop-stich panels use a coated fabric. The skins of the drop-stich panel shown in Figure 1.1 are made of nylon with a neoprene coating.

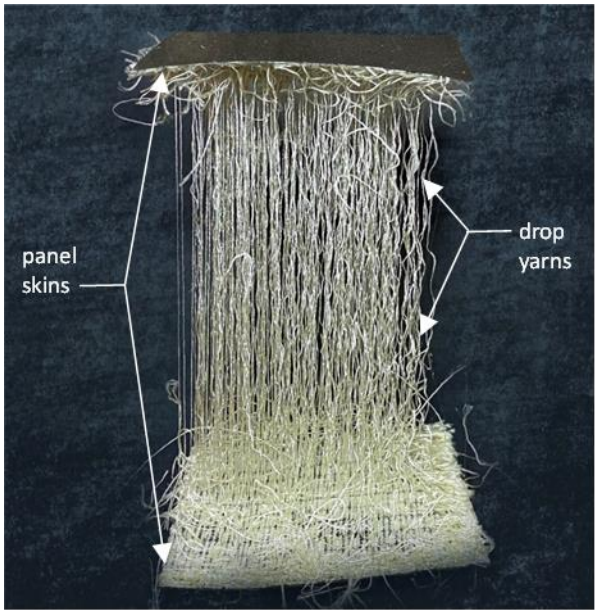

Figure 1.1: Drop-Stitch Sample

Wielgosz et al. (1998) and Wielgosz and Thomas (2002) refer to drop stitch panels as inflated fabric panels. In Wielgosz et al. (1998), experimental testing was conducted on drop-stitch panels made with two coated linen cloths connected by yarn. Three-point bend testing on different sized panels were used to develop a simplified model. These results were used to prove that it is possible to compute the behavior of drop stitch panels. With the knowledge that inflatable panels cannot be modeled as Euler Bernoulli beams, Wielgosz and Thomas (2002) used the experimental results and treated the inflatable panels as a Timoshenko beam to develop a new theory for inflatable panels. The experimental results prove the accuracy of this new theory when comparing the theoretical values. Wielgosz et al. (1998) and Wielgosz and Thomas (2002) both focus on the bending responses of the drop-stitch panels and treat the panels as an isotropic material.

Falls and Water (2011) experimentally tested four different drop-stitch panels of different thicknesses and widths in three-point bend tests. The bending deflections were

compared to the behavior of standard Euler-Bernoulli beams. Falls and Water (2011) came to three major conclusions: there is significant hysteresis in bending, bending stiffness is affected by inflation pressure and the cross-section of the panel, and similar to inflatable airbeams and arches, drop-stich panels should not be compared to Euler-Bernoulli beams. "The bending stiffness of the inflated specimens is not directly proportional to the second moment of inertia of the cross-section, as it is for Euler-Bernoulli beams" (Falls and Water, 2011). CDI Corp. provided the panels for this study but did not specify the manufacturer or the materials of the panel.

DiGiovanna (2013) studied drop-stich panels with a specific reference to stand up paddleboards. In this study, a small drop-stitch panel was fabricated in-house and the elastic modulus was estimated from deflection data. The data was collected using three-point bend tests at 25psi and 30psi. When the pressure was held at a constant, the estimated modulus from the developed model in this research was decreasing with time and a negative effective modulus was calculated. The effective modulus cannot be negative, therefore this research concluded that the elastic modulus could not be accurately determined using the in-house fabricated specimen.

Cavallaro et al. (2013) conducted analytical and experimental studies on drop-stich panels subject to bending loads. The analytical solution presented assumed that "the spatial density of the drop yarns, […], is sufficient, so that localized skin bowing deformation between adjacent drop yarns have a negligible effect on volume changes" (Cavallaro et al., 2013). The experimental testing consisted of uniaxial tension testing where the elastic modulus of the skin was estimated. The skin modulus, the ratio of biaxial tension stress, N_{ratio}, and the Poisson's ratio were used to determine the effective modulus. The tensile

strength of the drop yarns as individual yarns and in a woven state were also tested. Previous work on drop-stich panels included a three-point bend test. Cavallaro et al. (2013) utilized four-point bend tests to obtain the onset wrinkling moment. The analytical solution correlated well with the load-deflection results in four-point bending, but underestimated the ultimate bending load for low pressures.

Felicissimo (2015) conducted tension and shear tests on drop-stich panels. This study explored methods to determine the elastic modulus and shear modulus of both rigid and inflated drop-stitch panels. The method used focused on the effects from the drop-yarns. The torsion testing clamps a swatch of the material at the top and bottom membranes and then slowly separates the two membranes pulling on the drop-yarns. The shear tests were also conducted on a swatch of the material and the inflatable specimen was sealed in a pressurized containment system. This study concluded there are differences in the constitutive properties along both orthogonal planes, but states that for inflated specimens, the difference is less than 2% and therefore can be treated as transversely isotropic.

Unlike previous research on drop-stitch panels, Buglio (2020) incorporated digital image correlation (DIC) systems into the data acquisition methods. Brayley (2011), Brayley et al. (2012) and Clapp et al. (2015) are a few studies on inflatable structures that have utilized DIC technology in the past. Buglio (2020) conducted uniaxial, biaxial, panel inflation and four-point bend tests to determine the constitutive properties for a commercial PVC drop-stitch panel. The goal of this study was to provide data to help improve understanding of the mechanical response of drop-stitch inflatable panels.

The research on inflatable structures has come a long way in the past 20 years. As shown above, the majority of the literature focuses on inflatable structures with a circular

cross-section. While bending test of drop-stitch panels have been reported, much of the work done on drop-stitch inflatable panels has focused on the accurate determination of constitutive properties to help develop accurate modeling and a better understanding of the drop-stitch technology. To-date, however, no study has definitively and accurately linked the experimental determination of panel skin constitutive properties with panel bending response. Further, the assessment of post-wrinkling response has not been extensively addressed.

1.2 Thesis Objective and Tasks

The primary objective of this research is to develop testing procedures to determine the constitutive properties of orthotropic neoprene/nylon drop-stitch inflatable panels fabric and panel load-deflection response on bending. Through four major tasks, the primary objective was achieved.

1. Through panel inflation and skin coupon testing, determine the effective panel orthotropic constitutive properties in the longitudinal/warp and transverse/weft directions of the panel.
2. Through large-scale torsion test, determine the membrane shear modulus.
3. Conduct full-scale panel bending tests to large displacements to quantify panel bending load-deflection response and the effect of inflation pressure on panel stiffness and capacity.
4. Compare large-scale bend test load-deflection behavior with response estimated using experimentally-determined skin constitutive properties.

1.3 Contributions of Thesis

The research in this thesis focuses on the specific material properties of a drop-stitch inflatable panel made of neoprene and nylon. This research also contributes to developing testing protocols for determining the constitutive properties of drop-stitch inflatable panels made of any material. These tests were developed for the data to be repeatable and comparable to other drop-stitch panels.

1.4 Organization of Thesis

This thesis is organized into six chapters including this introductory chapter. Chapter 2 gives details of the panels assessed in this study and also included details of coupon-level testing of the panel fabric skins. This chapter also includes a description of the test procedure, specimen preparation, an explanation of digital image correlation systems, and the determination of Poisson's ratio. Chapter 3 provides experimental results for panel inflation testing as well as the experimental results from torsion testing. This chapter also includes a description of both test procedures, an explanation of the torsion testing apparatus, and an explanation for determining the longitudinal/warp and transverse/weft membrane moduli and the membrane shear modulus.

Chapter 4 provides experimental results from four-point bend testing, including testing procedures, apparatus design, an explanation for estimating the onset wrinkling and deflection. A critical discussion of the result and comparison with response predicted in the pre-wrinkling range is also provided. Chapter 5 provides a summary and recommendation for future research.

CHAPTER 2

INITIAL MEASUREMENTS

2.1 Panel Description

Drop-stitch panels incorporate yarns stitched between the top and bottom layers of the panel through the thickness. The architecture of the specimens used in this research from top to bottom is neoprene/ nylon/ neoprene/ nylon/ yarns/ nylon/ neoprene/ nylon/ neoprene. The two panels that the Advanced Structures and Composites Center received from NAVATEK are identical except for the spacing of the air ports. The NAVATEK DWG NO. K459-1400-001, REV A, with configurations A and B is given in Figure 2.1 below. The identifier for these panels will be K459. All dimensions in this figure are nominal, and measured dimensions are provided later in this report. UMaine also received from NAVATEK a roll of the same neoprene/nylon fabric that was used to manufacture the panels.

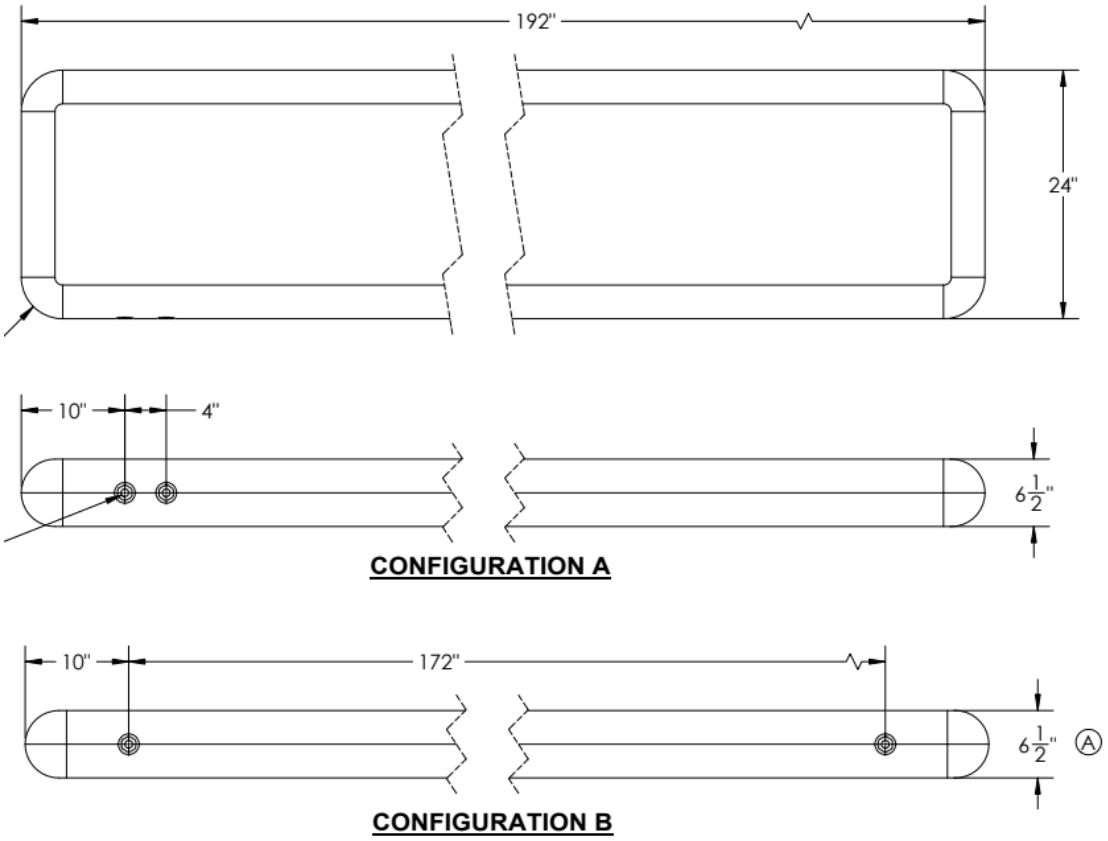

Figure 2.1: CAD Drawings of K459 Neoprene Panels

In Figures 2.2 through 2.7 below, both configuration A and configuration B for the neoprene panel can be observed at inflation pressures of 5, 15 and 30 psi. The images on the left show the panel resting on the ground, and in the images on the right, the farthest end of the panel is held level with a weight. Both configuration A and B show significant panel twist, but configuration B has more significant upward curvature along its length. Due to this additional curvature in panel B, all panel testing was completed with only configuration A and is denoted as K459A.

Figure 2.2: Configuration A inflated to 5 psi

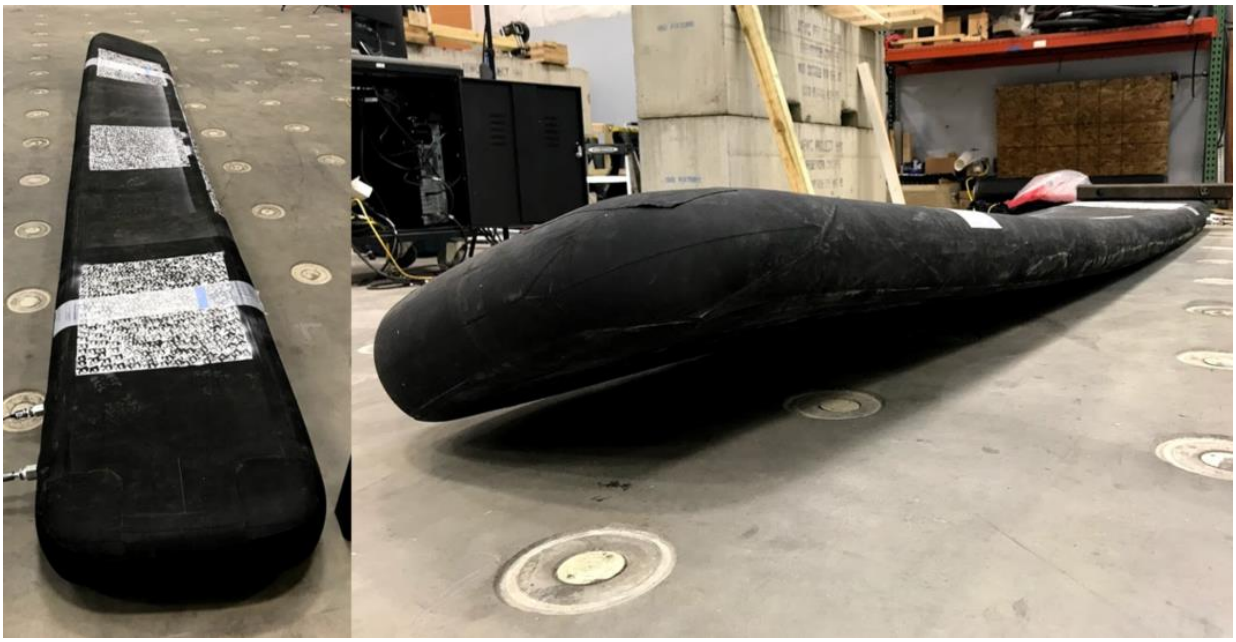

Figure 2.3: Configuration A inflated to 15 psi

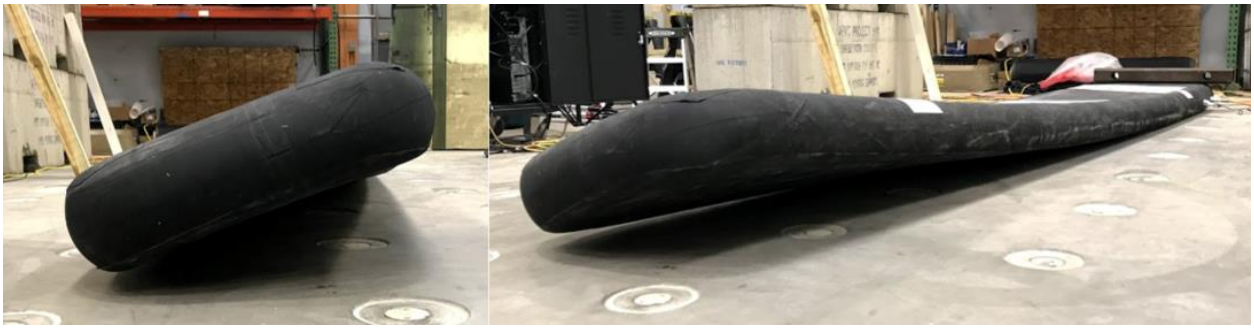

Figure 2.4: Configuration A inflated to 30 psi

Figure 2.5: Configuration B inflated to 5 psi

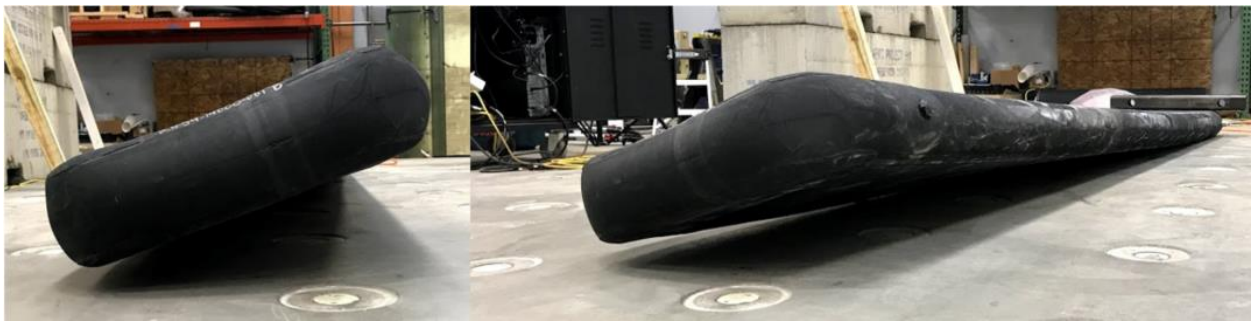

Figure 2.6: Configuration B inflated to 15 psi

Figure 2.7: Configuration B inflated to 30 psi

Actual panel dimensions were measured for 5, 10 and 15 psi on the top and bottom of the panel. The height, width, cross-sectional perimeter and gap in the panel were measured, and are presented below. For four-point bend testing, the initial curvature of the panel was measured, and is presented in Chapter 4. A piece of wood was placed on the top of the panel with a level near the area of measurement to ensure the panel was flat on the

floor when taking measurements. The height was measured from the floor to the piece of wood and the width was measured on the flat portion of the panel from seam to seam. The gap between the center of the panel and the flat piece of wood resting on top was measured with a feeler gauge. The cross-sectional perimeter was then measured using a piece of string wrapped around the panel, then the length of the string was measured on a tape measure. All panel dimensions are presented below in Table 2.1 through Table 2.3. The averages for all pressures can be found in Table 2.4. The locations for all measurements can be seen in Figure 2.8.

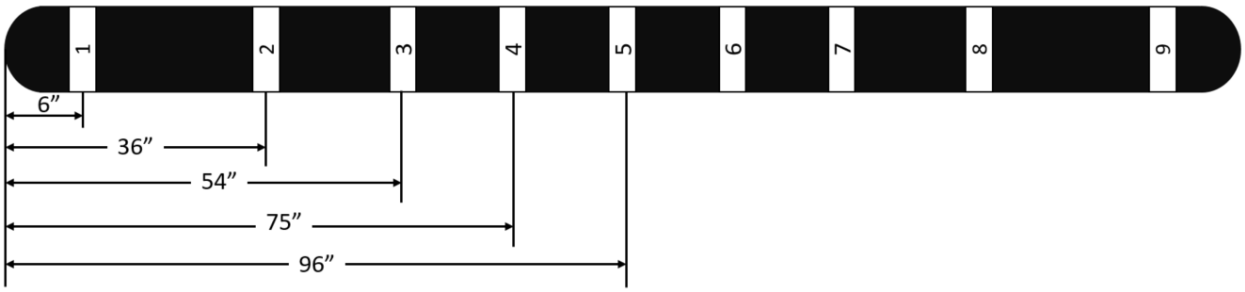

Figure 2.8: Approximate Locations for Panel Measurements

The numbers on the panel in Figure 2.8 represent the location on the panel where the measurements were taken, as presented in Tables 2.1 through 2.3 below. In these tables, “Port” represents the side of the panel where the inflation ports are located, and “Back” represents the other side of the panel.

Table 2.1: Panel K459A configuration A Measurements at 5 psi. (inches)

		1	2	3	4	5	6	7	8	9
Top	Port Height	6.938	6.875	6.875	6.875	7.125	6.875	6.812	6.875	7.125
	Back Height	6.875	6.875	6.875	6.938	6.875	6.938	6.875	7.125	6.875
	Width	22.56	22.50	22.44	22.38	21.94	22.62	22.50	22.69	22.00
	Gap	0.132	0.114	0.147	0.147	0.091	0.177	0.144	0.157	0.015
Bottom	Port Height	6.938	6.875	6.938	6.938	6.938	6.875	7.250	7.188	7.375
	Back Height	6.875	6.875	6.750	6.938	7.062	6.875	6.688	6.750	7.125
	Width	22.50	22.50	22.31	22.38	22.06	22.50	22.44	22.50	21.81
	Gap	0.163	0.179	0.102	0.120	0.141	0.130	0.140	0.132	0.278
Cross-Sectional Perimeter		65.25	65.00	64.31	64.25	63.12	65.38	65.44	65.19	63.25
Full Width (w_0)		28.75	28.50	28.31	28.13	27.75	28.25	28.56	28.50	27.94

Table 2.2: Panel K459A configuration A Measurements at 10 psi (inches)

		1	2	3	4	5	6	7	8	9
Top	Port Height	7.188	7.000	7.250	7.250	7.312	7.125	6.938	6.875	7.000
	Back Height	6.938	6.938	7.000	6.938	6.875	6.938	7.000	7.500	7.062
	Width	22.81	22.69	22.44	22.06	22.06	22.68	22.62	22.62	22.06
	Gap	0.167	0.156	0.185	0.155	0.138	0.205	0.178	0.193	0.010
Bottom	Port Height	6.938	6.875	7.000	7.000	6.938	7.000	7.250	7.250	7.312
	Back Height	7.375	7.125	7.250	7.250	7.062	7.000	6.875	6.938	7.375
	Width	22.50	22.62	22.50	22.31	22.19	22.56	22.62	22.56	22.06
	Gap	0.125	0.156	0.083	0.112	0.134	0.130	0.151	0.098	0.220
Cross-Sectional Perimeter		65.50	65.25	64.88	64.75	63.50	65.31	65.38	65.12	63.75
Full Width (w_0)		28.94	28.75	28.56	28.25	28.00	28.88	28.94	28.88	28.00

Table 2.3: Panel K459A configuration A Measurements at 15 psi. (inches)

		1	2	3	4	5	6	7	8	9
Top	Port Height	7.312	7.250	7.375	7.500	7.375	7.250	7.062	6.938	7.062
	Back Height	7.062	7.062	7.062	7.125	7.188	7.000	7.062	7.500	7.188
	Width	22.88	22.81	22.69	22.56	22.25	23.00	22.81	22.88	22.25
	Gap	0.165	0.150	0.192	0.240	0.130	0.203	0.179	0.211	0.000
Bottom	Port Height	7.000	7.000	7.062	7.250	7.062	7.000	7.062	7.188	7.375
	Back Height	7.188	7.188	7.250	7.312	7.188	7.125	7.125	6.938	7.500
	Width	22.88	22.94	22.75	22.75	22.50	22.75	22.81	22.88	22.25
	Gap	0.138	0.157	0.116	0.100	0.148	0.112	0.122	0.100	0.224
Cross-Sectional Perimeter		66.25	66.12	65.62	65.50	64.38	66.00	65.94	66.25	64.50
Full Width (w_0)		29.25	29.06	28.63	28.38	27.88	29.13	29.13	29.00	28.25

Table 2.4: Panel K459A Left, Mid-Span and Right Average Measurements (inches)

	5 psi			10 psi			15 psi		
	Left	**Mid-Span**	**Right**	**Left**	**Mid-Span**	**Right**	**Left**	**Mid-Span**	**Right**
Height	6.906	6.875	6.891	7.109	6.984	7.016	7.141	7.125	7.094
Width	22.53	22.50	22.56	22.66	22.66	22.63	22.88	22.88	22.88
Gap	0.1476	0.1465	0.1533	0.1459	0.1559	0.1673	0.1514	0.1533	0.1575
Cross-sectional Perimeter	65.25	65.00	65.38	65.50	65.25	65.31	66.25	66.12	66.00
Full Width (w_0)	28.75	28.50	28.25	28.94	28.75	28.88	29.25	29.06	29.13

A diagram of the panel cross-section can be seen in Figure 2.9 below. The transverse/weft direction is represented by the z-axis, the longitudinal/warp direction are out the page in the x-axis, and the y-axis is through the thickness of the panel.

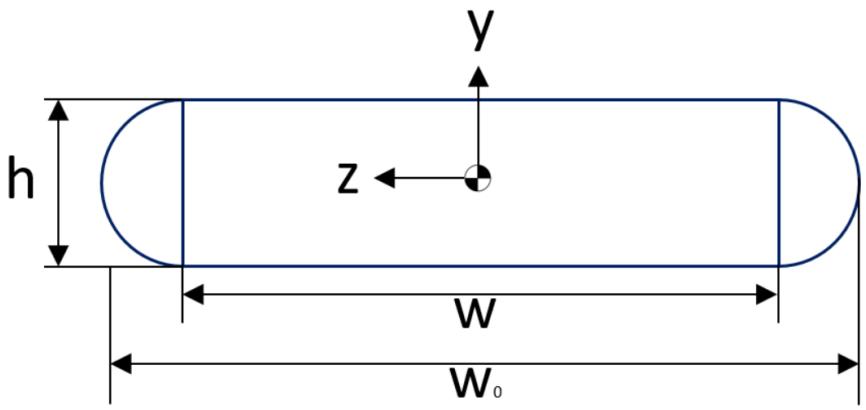

Figure 2.9: Diagram of Panel Cross-Section

2.2 Digital Imaging Correlation System

Digital Imaging Correlation (DIC) systems are used to measure stain. Two cameras are set to 20˚ and -20˚ facing the specimen that has a speckled paint pattern as seen in Figure 2.10. The two cameras take photos simultaneously, then using a DIC system (ARAMIS or GOM Correlate), the pixels in the speckled pattern painted on the specimen are tracked and the DIC system estimates the strain in both the x- and y-directions.

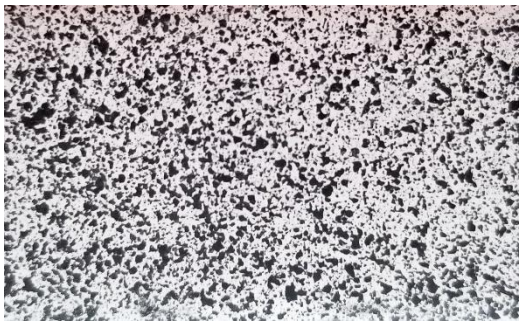

Figure 2.10: Speckled Paint Pattern

2.3 Coupon-Level Testing

Coupon-level tension testing is traditionally used to determine Young's modulus, E, and the Poisson's ratio, ν. Due to the dependence of fabric modulus on inflation

pressure, the orthotropic membrane moduli are calculated using stress-strain data from inflation testing (see Chapter 3), Poisson's ratio ν_{xz} and assuming the panel skin behaves as an orthotropic material. Poisson's ratio is determined from the coupon-level testing detailed here. While not directly applicable for the drop stitch panel, the longitudinal modulus based on the coupon tests results is reported for comparison with the more realistic moduli determined from inflation testing as detailed in Chapter 3.

All moduli reported here are membrane values, which are directly related to Young's Modulus, E, by the thickness of the material *t* as shown in Equation 2.1.

$$E^* = E \cdot t \tag{2.1}$$

The membrane modulus is convenient for fabrics; the thickness is very small and may be difficult to measure or is inconsistent.

2.3.1 Preparing the Specimens

Cutting the Specimen

To test the supplied material, coupons were cut to a dimension of 1x12in. The dimensions of the specimens were determined by the size of the initial panel swatch that was received from NAVATEK to develop the testing procedures. The swatch was 2 ft by 1 ft. Specimens were cut for testing in both the longitudinal/warp and transverse/weft directions.

Originally, specimens were cut using an aluminum stencil and a straight razor. However, this method of cutting the coupons did not provide straight edges and consistent dimensions. To improve specimen quality, coupons were subsequently cut using a waterjet cutter. A waterjet can cut specimens with an accuracy of approximately 0.003 in. However,

one concern with cutting fabric coupons on the waterjet is the effect on the properties of the nylon fabric.

Nylon is a hygroscopic material, which means that it can easily absorb moisture from its surroundings. Prior research has shown that high moisture content can reduce the strength and stiffness of nylon while increasing energy absorption capability and ductility of the material (BASF Corporation, 2003). However, once the nylon has dried completely, the properties will return to their original state. In some cases where there are extremely high temperatures and high saturation, there could be significant changes in the properties (Puls, 1947; Miri, 2009). The materials used in this study were not processed or tested at high temperatures. This indicated that coupons cut on a waterjet would have acceptable properties provided the specimen has been dried completely after cutting.

Before putting the material swatch on the waterjet, the volume, *V*, was approximated and the mass *m* was found to determine the density ρ as seen in Equation 2.2.

$$\rho = \frac{m}{V} \tag{2.2}$$

Once the material was cut on the waterjet, the volume subsequently changed. The kerf of the water jet is approximately 0.04 in. To approximate the new volume of the material swatch, the kerf and the perimeter of the cut were used. This resulted in a volume reduction of 3.4-4.7%. The material was weighed immediately after being taken from the waterjet and a new density was calculated. The material was then placed in a temperature and humidity controlled room set at 70˚ and 50% RH. After a few days, the material was weighed again and a new density was calculated. This new density calculation was

compared to the initial density to determine is the specimen has fully dried. It was found that two to three days in the temperature and humidity controlled room was a sufficient amount of time for the specimen to completely dry, which occurred when the density was within ±1% of the originally measured value.

Painting and preconditioning the specimens

After the coupon specimens had been dried completely, the speckle paint pattern for the DIC system was applied. Originally, VALSPAR interior latex paint was used as a white base. When tested on some sample specimens, the paint cracked under specimen elongation due to the high compliance of the fabric. Due to this, other paints or coating were assessed for the use as a white base that is more suitable for the fabric specimens. One such product is UreCoat® by SMOOTH-ON. UreCoat® is a flexible urethane coating that can be painted on to the surface. According to the manufacturer's specifications (Smooth-On, n.d.) it has a tensile strength of 1,360 psi and an elongation at break of about 876%. The downside of this option is the preparation time for each specimen. UreCoat® only has a pot life of 8 minutes, and requires 16 hours to cure. Another downside is that the product comes clear with a glossy finish, and colorant must be added. A glossy finish has negative effects on the DIC system, and while a matte finish can be achieved, it requires additional preparation. Another option that was explored was Rust-Oleum white flat acrylic enamel, which proved to work very well and was used for all testing reported here, as the maximum strain measured was about 15%. After prepping, all specimens were preconditioned for at least 24 hours before being tested by leaving them in a temperature and humidity controlled room held at 70˚F and 50% RH.

2.3.2 Coupon Test Protocol and Load Calculations

All coupons were tested on an Instron machine with a 1 kip load cell, using a load rate of 7 lb/sec. To ensure repeatable results, each specimen was subjected to 10 cycles at two different loads. One set of specimens was tested at loads that represented the stresses seen by inflation pressure only. A second set was loaded to a higher level that took the additional stresses caused by bending during four-point bend testing into consideration.

Similar to elastic modulus, the membrane stresses are defined as the product of the stresses σ and membrane thickness t (Equation 2.3) and have units of force per unit width.

$$\sigma^* = \sigma \cdot t \tag{2.3}$$

The stress due to inflation pressure, p, in the longitudinal/warp direction is illustrated in Figure 2.11.

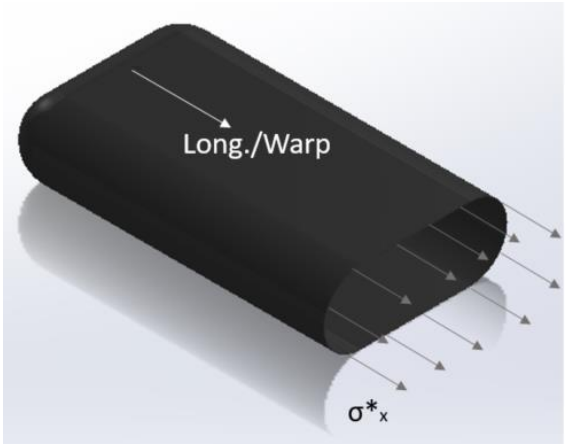

Figure 2.11: Cross section of a panel cut in the weft direction

As seen above in Figure 2.9, the cross-section of the panel is idealized as a rectangle with two half-circles. The longitudinal/warp stress σ_x^* can be determined by equating the pressure force to the membrane stress on a cross-section. That is,

$$p\left(\frac{\pi h^2}{4} + wh\right) = \sigma_x^*(\pi h + 2w)$$

Therefore, the longitudinal/warp stress can be written as Equation 2.4 below.

$$\sigma_x^* = \frac{p(wh + \pi h^2/4)}{2w + \pi h} \tag{2.4}$$

Similarly, the membrane stress due to inflation pressure in the transverse/weft direction is found by considering the section shown in Figure 2.12.

$$p \cdot h \cdot \Delta z = \sigma_z^*(2 \cdot \Delta z)$$

Therefore, the transverse/weft stress can be written as Equation 2.5 below.

$$\sigma_z^* = \frac{ph}{2} \tag{2.5}$$

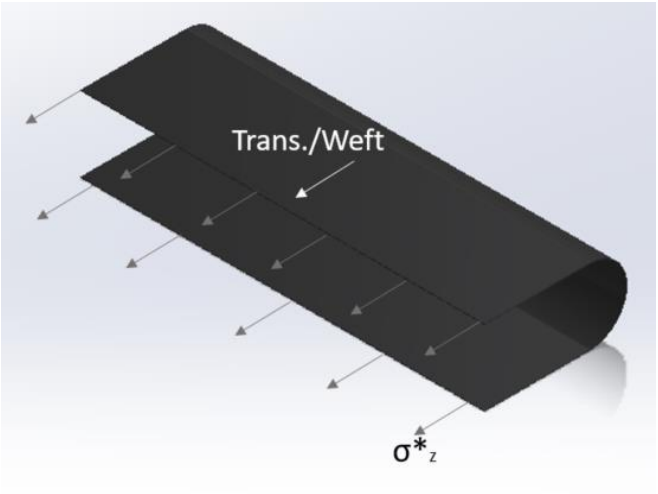

Figure 2.12: Cross-Section of a panel cut in the warp direction

The maximum inflation pressure for the given panels is 30 psi, with a typical operating pressure of 15 psi. To calculate the loads for coupon testing, the operating range was used. Membrane stress is force per with width, therefore the corresponding load, *F*, will be stress multiplied by the width of the coupon (Equation 2.6), which is 1 in. The width of the coupon was determined using ASTM D3039/D3039M.

$$F = \sigma^* \cdot (1\ in) \tag{2.6}$$

As mentioned above, one set of specimens was tested only considering the stresses due to inflation pressure. For the longitudinal/warp direction, the max calculated load is 90 lb, therefore for this 1st set, the specimens went through ten cycles from approximately 0 to 45 lb, then ten additional cycles from approximately 0 to 90 lb. To account for the bending stresses, the load due to inflation pressure was multiplied by a factor of 3. While the maximum stress caused by bending at the point when the fabric on the compression face of the panel loses tension (wrinkles) is twice the stress seen from inflation pressure, an additional multiplier was applied to ensure that coupon test fully assesses the stress range of the fabric. Therefore, the max calculated load for the second set of specimens is 270 lb. For this set, the specimens are taken to a max of 130 lb for ten cycles, and then taken to a max of 270 lb for an additional ten cycles.

2.3.3 Results

The nomenclature for the coupons represents the panel identifier (K459A), the approximate panel thickness (7 in), the direction of the cut, and the test number. The abbreviations for the direction of cut are “wp” for longitudinal/warp and “wt” for transverse/weft. Due to only being interested in the Poisson’s ratio ν_{xz}, specimens were

only tested in the longitudinal/warp direction. As mentioned above, there were two separate sets tested, there were five specimens in each set (Table 2.5)

Table 2.5: Coupon-Level testing sets

Set 1: Inflation Only	**Set 2: Inflation + Bending**
7wp10	7wp5
7wp11	7wp6
7wp12	7wp7
7wp13	7wp8
7wp14	7wp9

Figures 2.13 through 2.22 show the longitudinal/warp membrane stress vs strain, as well as the longitudinal/warp strain vs transverse/weft strain for all test specimens. As seen for all test specimens, there is significant hysteresis in each load/unload cycles.

The Poisson's ratio, ν_{xz}, is defined as Equation 2.7 below.

$$\nu_{xz} = -\frac{\varepsilon_z}{\varepsilon_x} \tag{2.7}$$

This relationship can be found by using a linear regression on the data in the Long./Warp vs Tran./Weft Strain graphs below. The Poisson's ratio for each test is presented in Table 2.6, as well as the average for both sets of specimens.

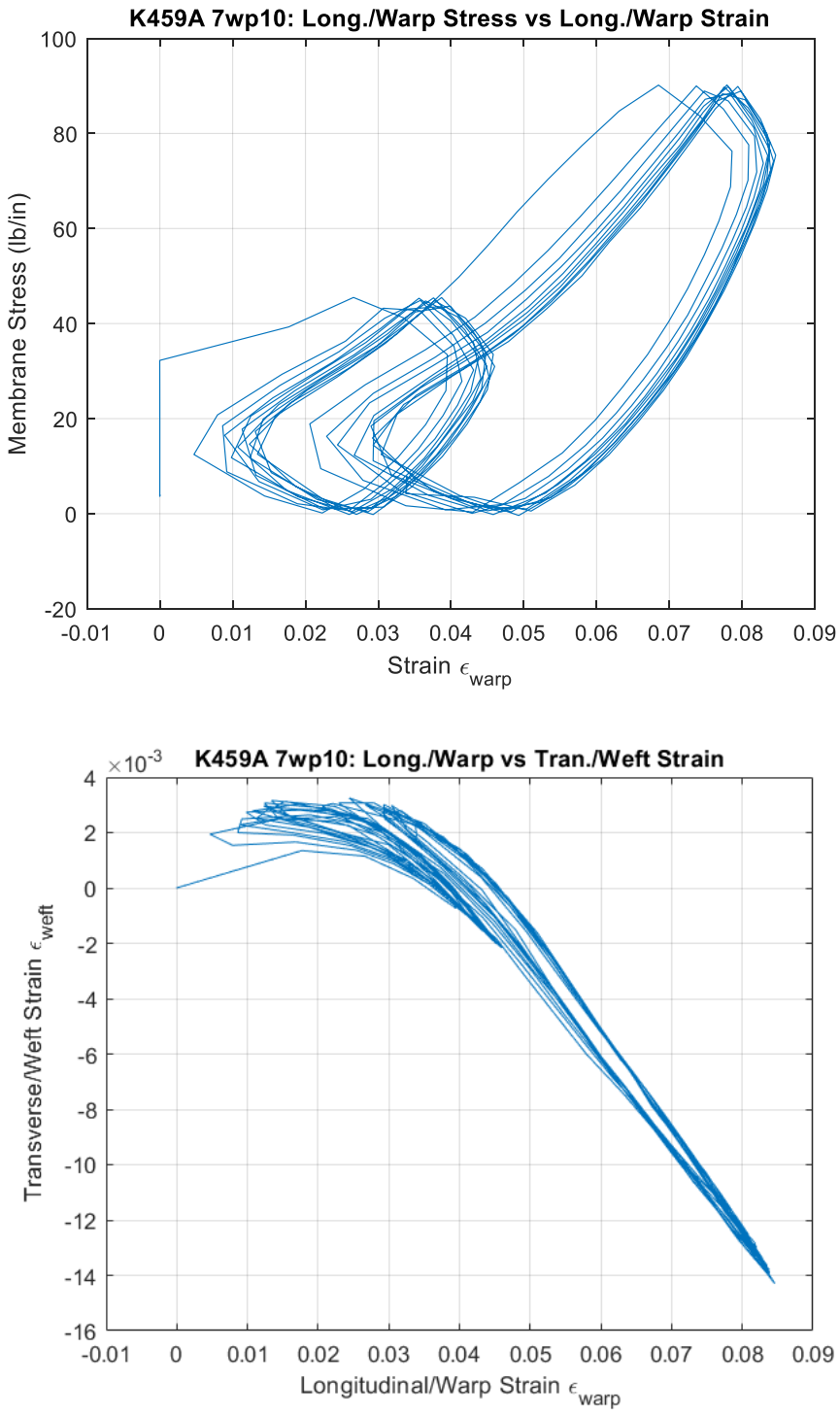

Figure 2.13: K459A 7wp10

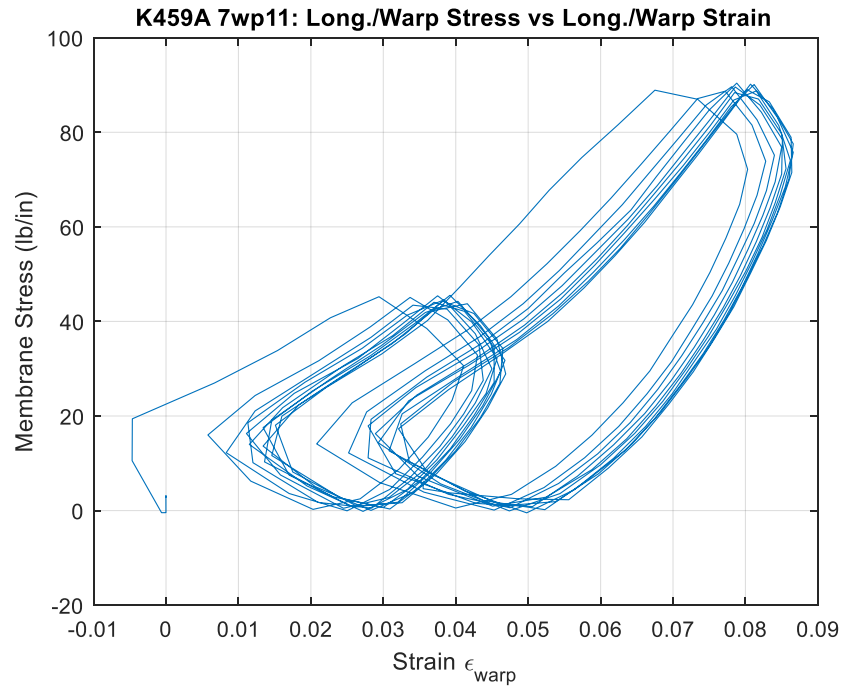

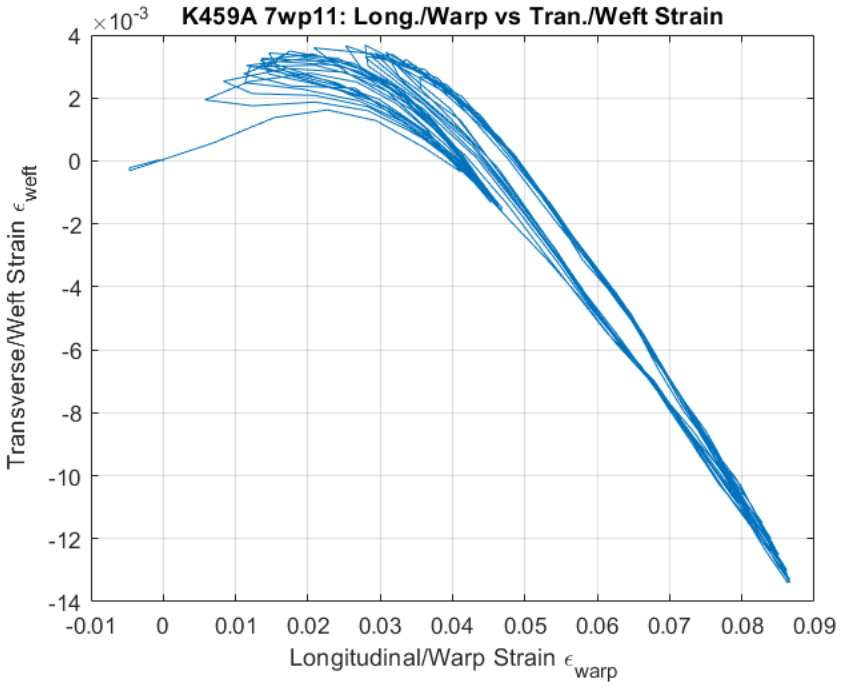

Figure 2.14: K459A 7wp11

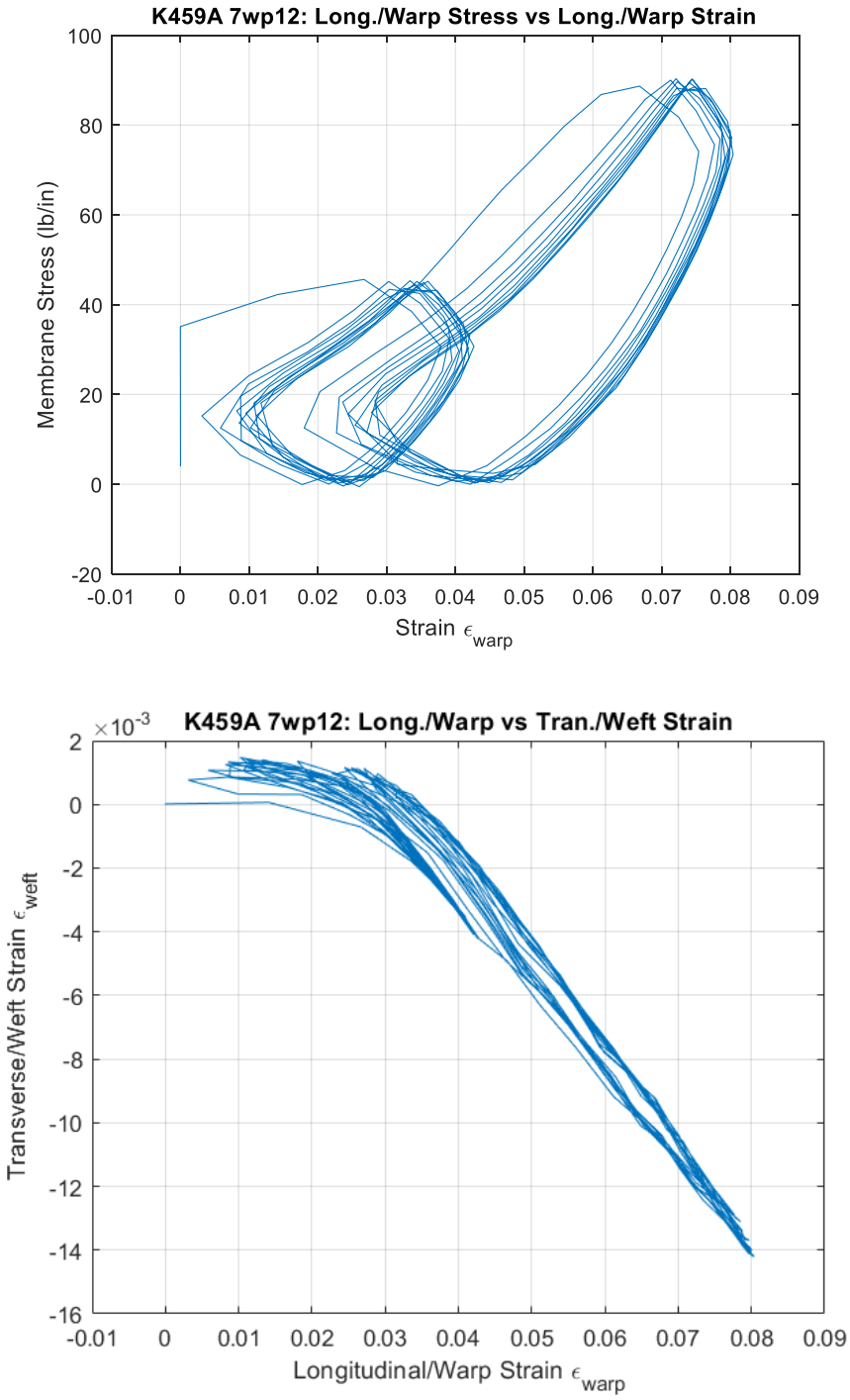

Figure 2.15: K459A 7wp12

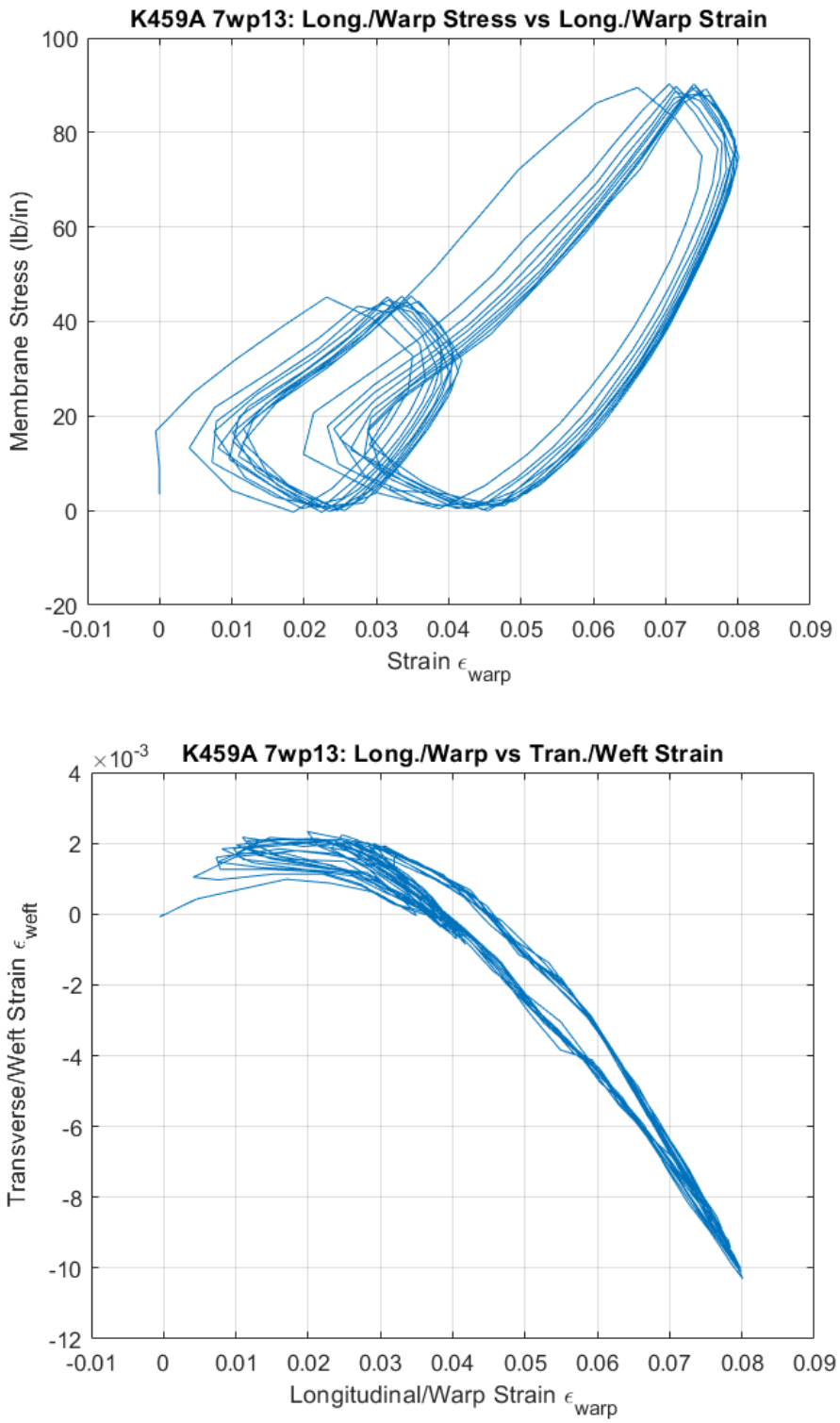

Figure 2.16: K459A 7wp13

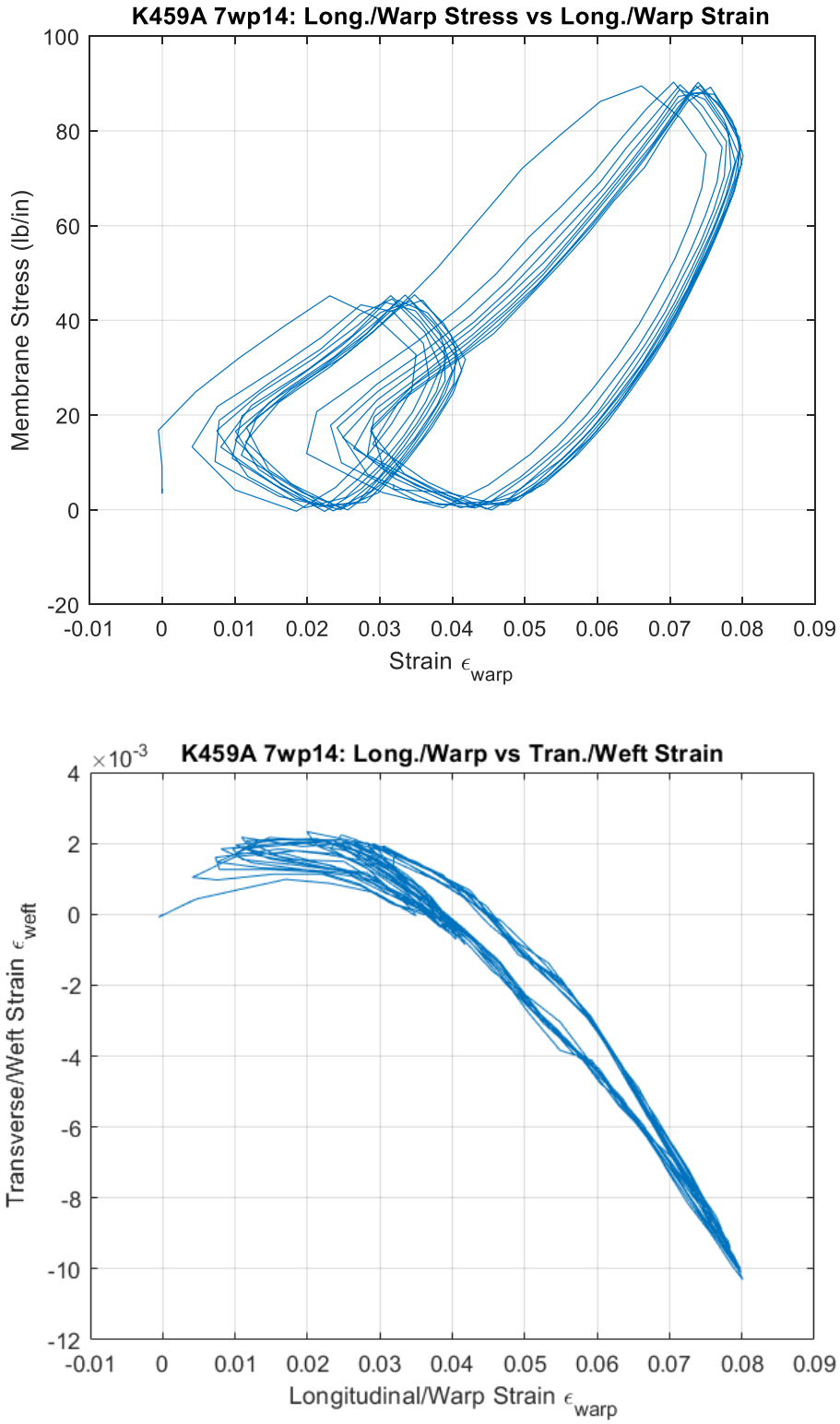

Figure 2.17: K459A 7wp14

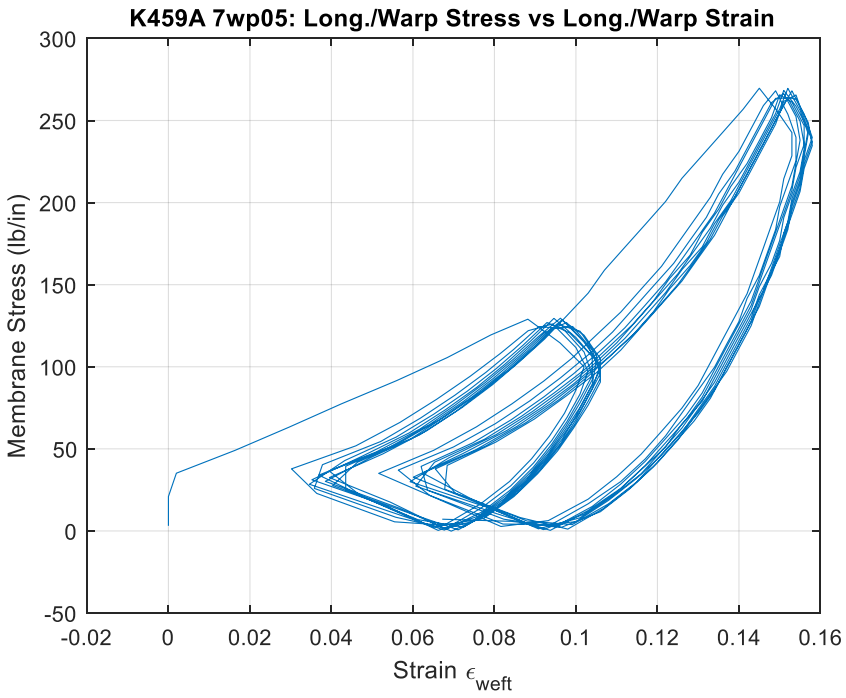

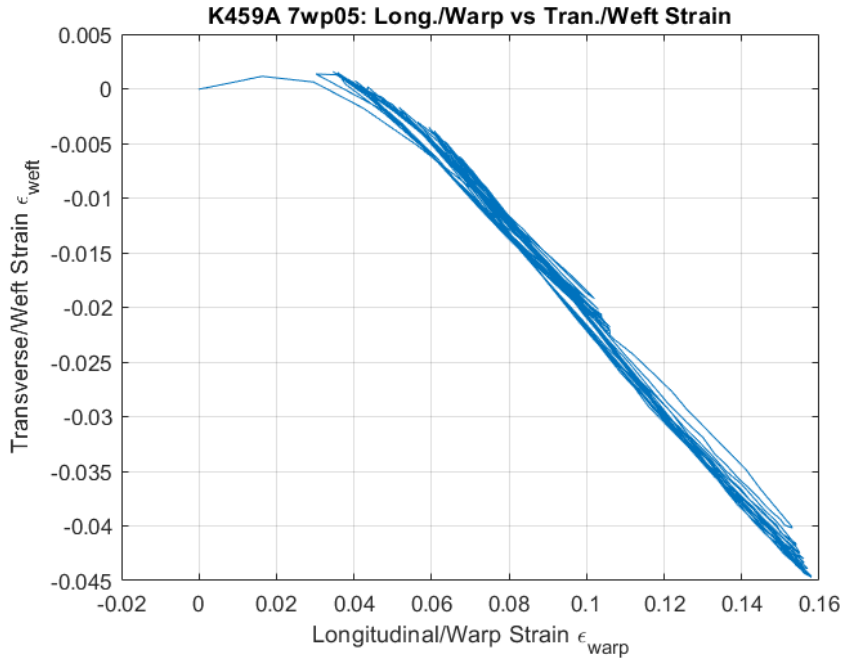

Figure 2.18: K459A 7wp05

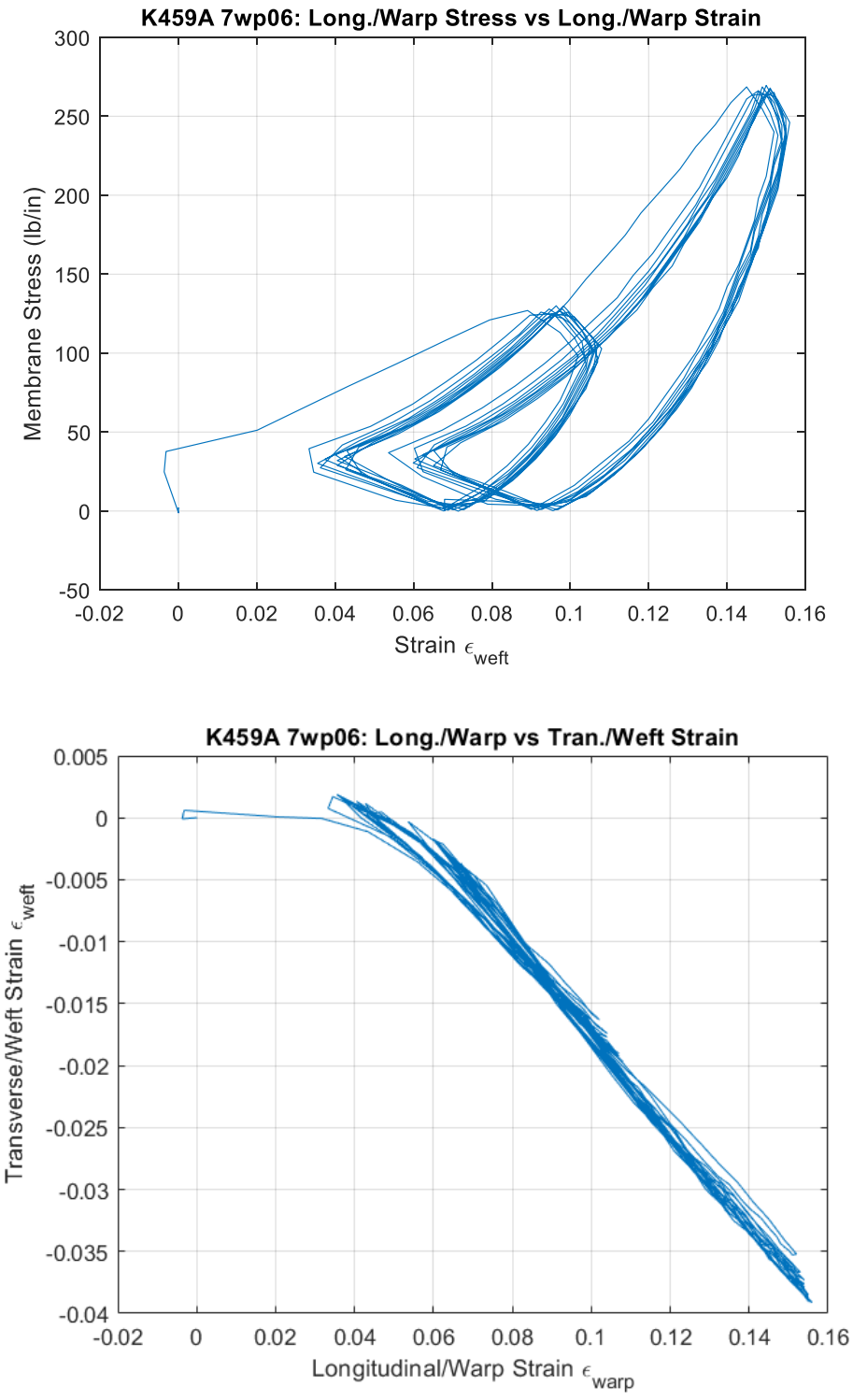

Figure 2.19: K459A 7wp06

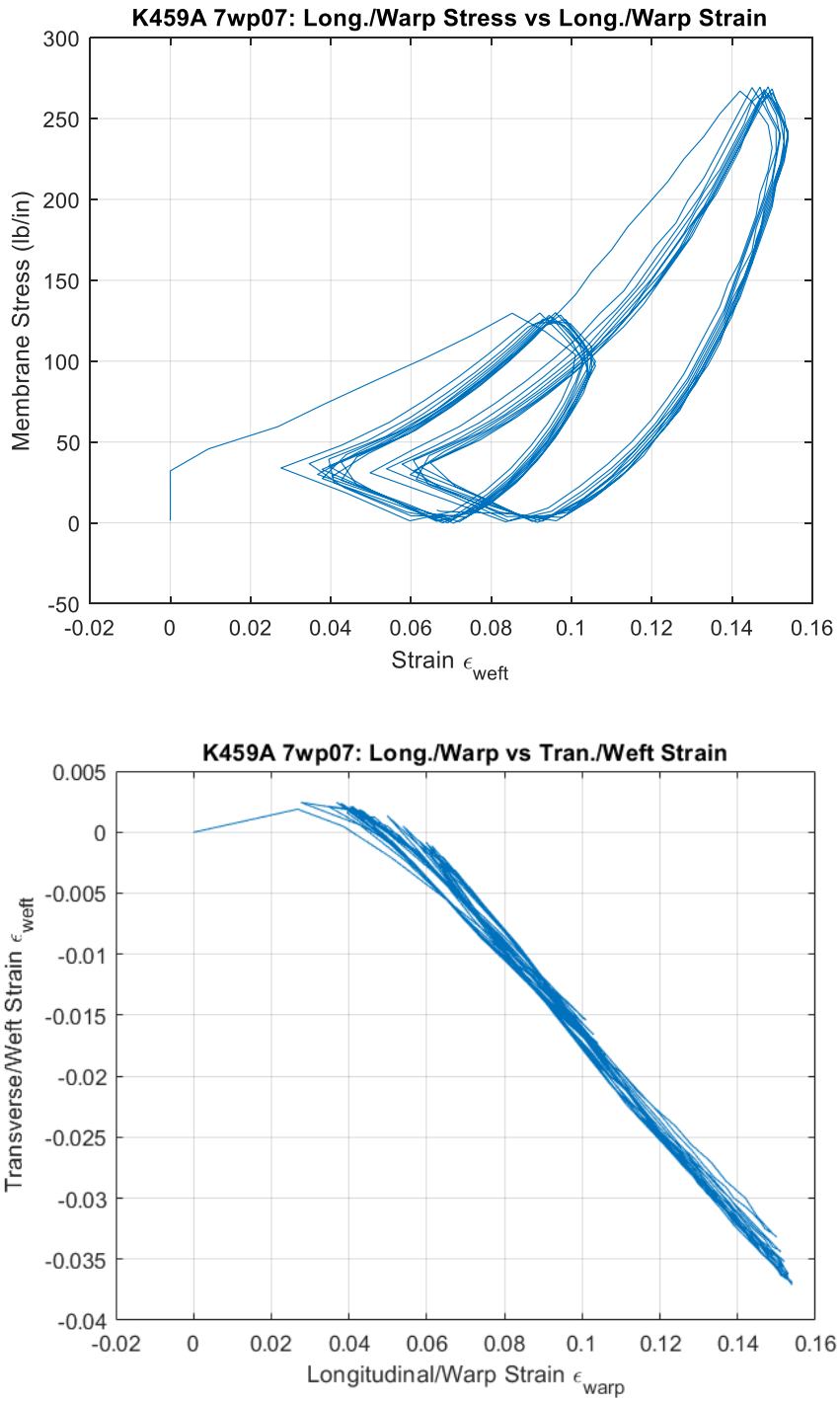

Figure 2.20: K459A 7wp07

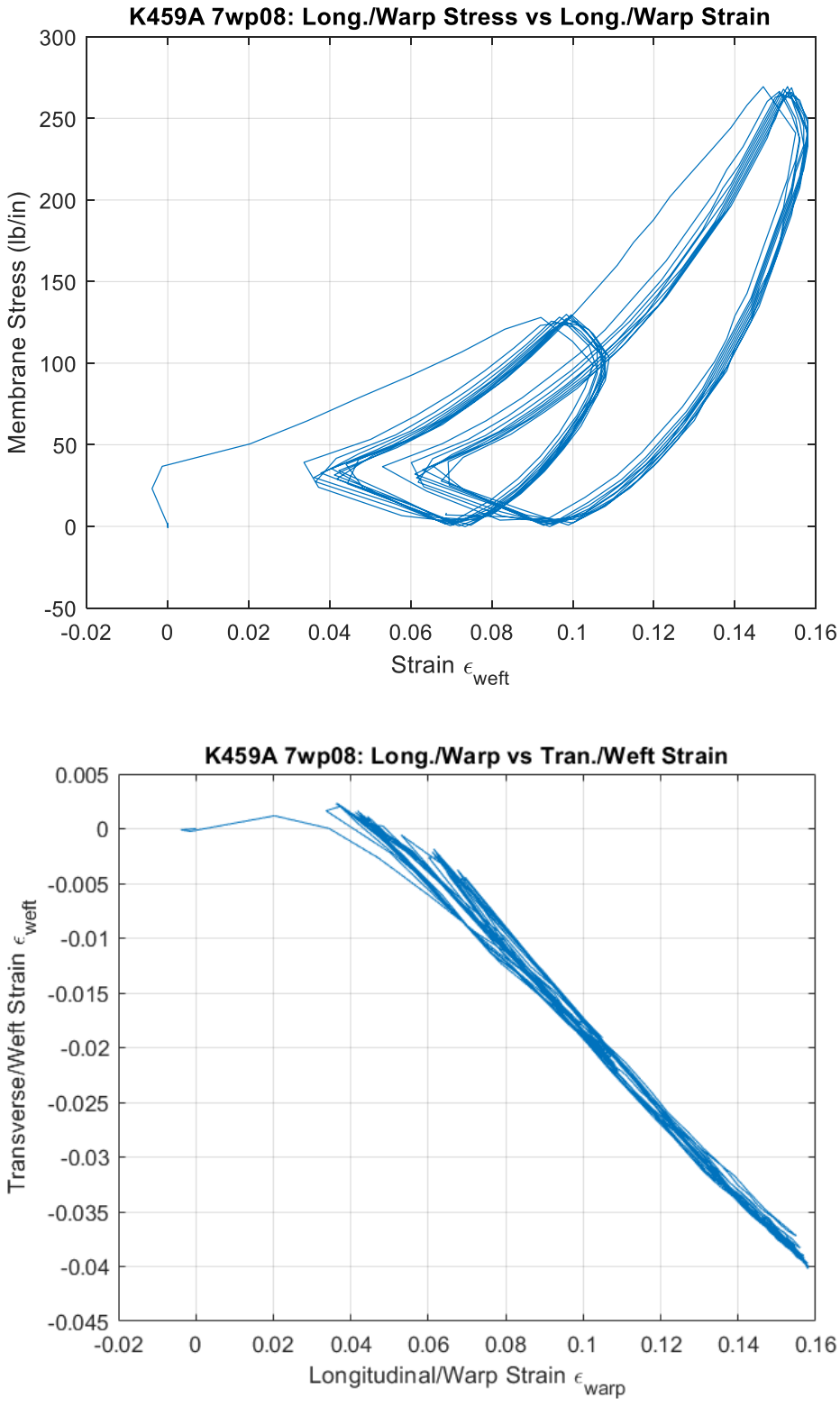

Figure 2.21: K459A 7wp08

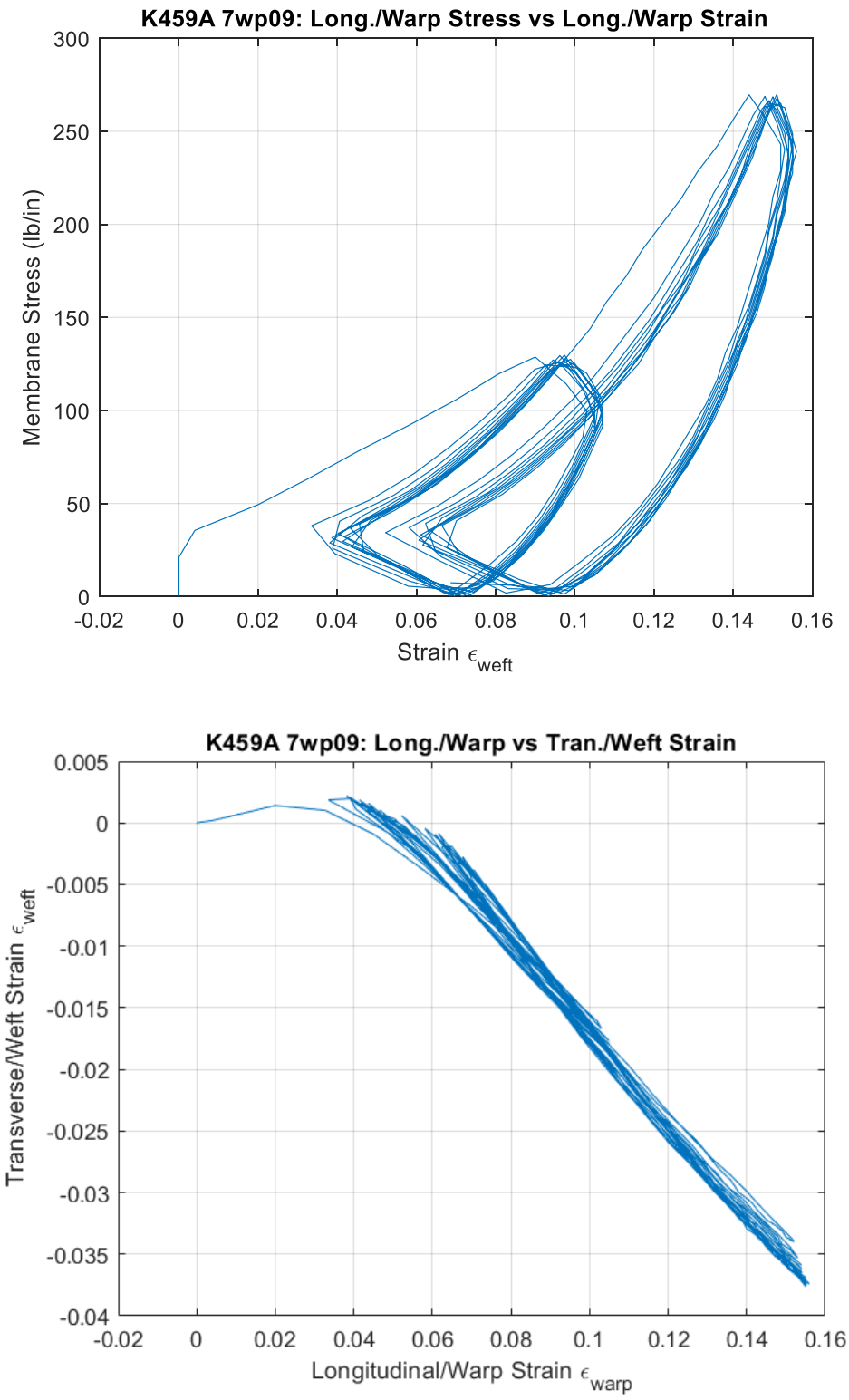

Figure 2.22: K459A 7wp09

Table 2.6: Poisson's ratio results

Upper Range (130 & 270 lb.)		Lower Range (45 & 90 lb.)	
Coupon	**Poisson's Ratio, ν_{xz}**	**Coupon**	**Poisson's Ratio, ν_{xz}**
7wp05	0.39	7wp10	0.34
7wp06	0.38	7wp11	0.32
7wp07	0.37	7wp12	0.30
7wp08	0.37	7wp13	0.26
7wp09	0.37	7wp14	0.25
Average	**0.38**	**Average**	**0.29**

As mentioned above, the longitudinal/warp modulus is estimated to compare to the membrane moduli calculated in Chapter 3 from inflation testing. The membrane modulus is defined in Equation 2.8 as the uniaxial stress over strain.

$$E_x^* = \frac{\sigma_x^*}{\varepsilon_x} \tag{2.8}$$

The Poisson's ratio computed from the lower range tests is used to determine the membrane moduli in Chapter 3. Therefore, for the comparison, the longitudinal/warp modulus is computed for the lower range specimens. This is done using a linear regression for the last 5 cycles for loads between 45 and 90 lb. The computed longitudinal/warp membrane modulus are reported in Table 2.7 for each test below.

Table 2.7: Long./Warp Modulus, E_x^*

Specimen	Long./Warp Modulus, E_x^* (lb/in)
7wp10	1821
7wp11	1802
7wp12	1840
7wp13	1877
7wp14	1876
Average	**1843**

Using a range of 45 to 90 lb represents an inflation range of 15 to 30 psi. Therefore, these values are comparable to the 15 to 30 psi range during inflation testing.

Chapter 3

MATERIAL PROPERTIES

3.1 Determination of Fabric Moduli

Prior testing of inflated fabric beams and the determination of effective fabric mechanical properties has shown that both the elastic and shear moduli increase with inflation pressure (Kabche et. al., 2011, Apedo et. al, 2010). This has been attributed to increased inter-tow friction and fabric de-crimping with increase inflation pressure (Kabche et. al, 2011). While the drop stitch panels tested here have a thick neoprene coating that may tend to reduce changes in fiber tow geometry, it is still expected that inflation pressure plays a role in fabric mechanical properties. This chapter details inflation testing and torsion testing that allow the estimation of the fabric elastic and shear moduli while incorporating pressure-dependence.

3.2 Calculation of Membrane Elastic Moduli from Inflation Tests

Unlike the coupon-level testing, the inflation testing creates biaxial stresses. Therefore, the calculation of the membrane moduli are more complicated. The compliance matrix (Equation 3.1) can be used to help determine the membrane moduli. Where the strain vector $[\varepsilon]$ equals the compliance matrix $[S]$ multiplied by the stress vector $[\sigma^*]$.

$$[\varepsilon] = [S][\sigma^*] \tag{3.1}$$

Equation 3.2 shows Equation 3.1 in the expanded form with all the terms defined.

$$\begin{bmatrix} \varepsilon_x \\ \varepsilon_z \\ \gamma_{xz} \end{bmatrix} = \begin{bmatrix} \frac{1}{E_x^*} & \frac{-\nu_{zx}}{E_z^*} & 0 \\ \frac{-\nu_{xz}}{E_x^*} & \frac{1}{E_z^*} & 0 \\ 0 & 0 & G_{xz}^* \end{bmatrix} \begin{bmatrix} \sigma_x^* \\ \sigma_z^* \\ \tau_{xz}^* \end{bmatrix} \tag{3.2}$$

In Equation 3.2 ε_x, E_x^* and σ_x^* are the strain, membrane modulus and the stress in the longitudinal/warp direction, while ε_z, E_z^* and σ_z^* are in the transverse/weft direction. γ_{xz} is shear strain, τ_{xz}^* is shear stress, and G_{xz}^* is the shear modulus. Inflation pressure only produces stresses in the longitudinal/warp and transverse/weft directions, but does not cause shear stress, and therefore $\tau_{xz}^* = 0$. The orthotropic symmetry relationship between ν_{xz} and ν_{zx} is given in Equation 3.3.

$$\nu_{zx} = \nu_{xz} \frac{E_z^*}{E_x^*} \tag{3.3}$$

Using Equation 3.3 and the fact that $\tau_{xz}^* = 0$ and shear is decoupled from the normal stresses, the elasticity relationships can be expressed as Equations 3.4 and 3.5 below.

$$\varepsilon_x E_x^* = \sigma_x^* - \sigma_z^* \nu_{xz} \tag{3.4}$$

$$\varepsilon_z E_z^* = \sigma_z^* - \sigma_x^* \nu_{xz} \frac{E_z^*}{E_x^*} \tag{3.5}$$

Equation 3.4 can be rearranged to Equation 3.6, providing a method for calculating the membrane modulus E_x^*. The changes in stress $\Delta\sigma_x^*$ and $\Delta\sigma_z^*$ are due to the change in inflation pressure, both of which are easily computed using the panel geometry as detailed previously in Chapter 2, and $\Delta\varepsilon_x$ is the measured change in the longitudinal/warp strain caused by the corresponding changes in stress $\Delta\sigma_x^*$ and $\Delta\sigma_z^*$. The Poisson's ratio ν_{xz} is known from the coupon-level testing detailed previously in Chapter 2.

$$E_x^* = \frac{\Delta\sigma_x^* - \Delta\sigma_z^* \nu_{xz}}{\Delta\varepsilon_x} \tag{3.5}$$

Once E_x^* is known, E_z^* can be determined using Equation 3.6. Similar to Equation 3.5, the changes in stress due to the change in inflation pressure are used, as well as the measured change in strain, but now for the transverse/weft direction.

$$E_z^* = \frac{\Delta\sigma_z^*}{\Delta\varepsilon_z + \frac{\nu_{xz}}{E_x^*}\Delta\sigma_x^*} \tag{3.6}$$

3.3 Testing Procedure

Similar to the coupon-level testing, the inflation testing utilizes the DIC software to measure the biaxial strains on the panel surface. On the side of the panel are two ports, one for the pressure hose, and the other for a pressure transducer. The pressure transducer has an output of 0-10V with a range of 0/60psi$_g$. The transducer was verified using a 5-point verification system. To control the pressure in the panel, a calibrated digital pressure readout attached to a pressure gauge was used (Figure 3.1). The pressure readout and gauge had a maximum pressure of 100 psi$_g$. As a safety guard a pressure gauge on the wall was set to 40 psi so the panel was not inadvertently over-pressurized.

Figure 3.1: Digital Pressure Readout and Pressure Gauge

To ensure consistency in the panel response, the panel is initially inflated to the working pressure of 15 psi and held overnight for at least 12 hours. The panel is then deflated to the initial pressure of the test. The bend testing conducted in Chapter 4 is done for pressure 5, 10 and 15 psi, where 15 psi is the normal operating pressure of the panel. Therefore, there are three pressure ranges tested 5 psi to 30 psi, the second 10 psi to 30 psi, and the last 15 psi to 30 psi. The upper limit of 30 psi was based on an estimate safe inflation pressure in the absence of other loading provided by the manufacturer. It is also equal to the theoretical stress in the panel skin at the onset of bending-induced wrinkling for an initial inflation pressure of 15 psi. Once the panel is at the initial pressure, it is inflated to the maximum panel inflation pressure of 30 psi as rapidly as possible. The inflation rate is dependent on the pressure apparatus used, and varied from approximately 200 to 300 seconds. The panel was then held at 30 psi for approximately 300 seconds. Figure 3.2 below shows the pressure vs time for 5 psi to 30 psi and held for 300 seconds for all tests. After the panel is held at 30 psi, it is then deflated back to the initial pressure. This cycle was completed three times to assess repeatability.

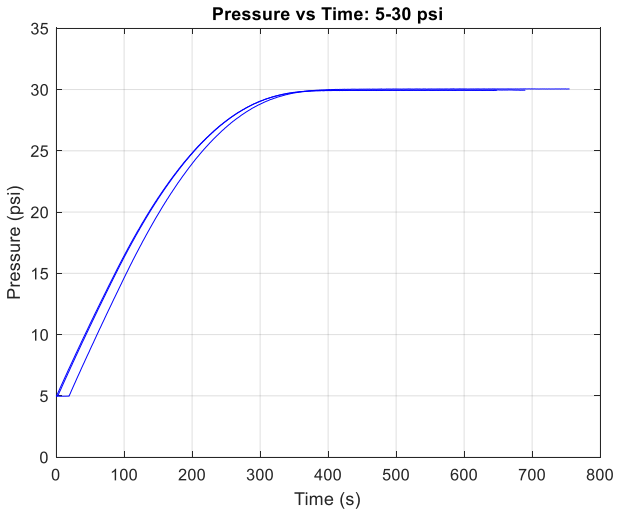

Figure 3.2: Pressure vs Time: 5-30 psi

3.4 Experimental Results

Figure 3.3 through 3.5 show the stress vs strain for both the longitudinal/warp and transverse/weft direction for all three pressure ranges. Using linear regression, an equation for the best-fit-line is determined for each test. To make each test comparable for a given range, they are each evaluated at two pressures to determine the change in stress and the change in strain, as seen in Table 3.1.

Table 3.1: Upper and Lower Pressures for all three ranges

	5-30 psi	**10-30 psi**	**15-30 psi**
Lower Pressure	5 psi	10 psi	15 psi
Upper Pressure	29.9 psi	29.9 psi	29.9 psi

The panel dimensions vary with inflation pressure, therefore the stresses must be determined for each inflation range despite all three ranges using an upper pressure of 29.9 psi. Utilizing the equation developed from the linear regression, the strain is computed. All changes in stress and strain are summarized in Tables 3.2 through 3.4.

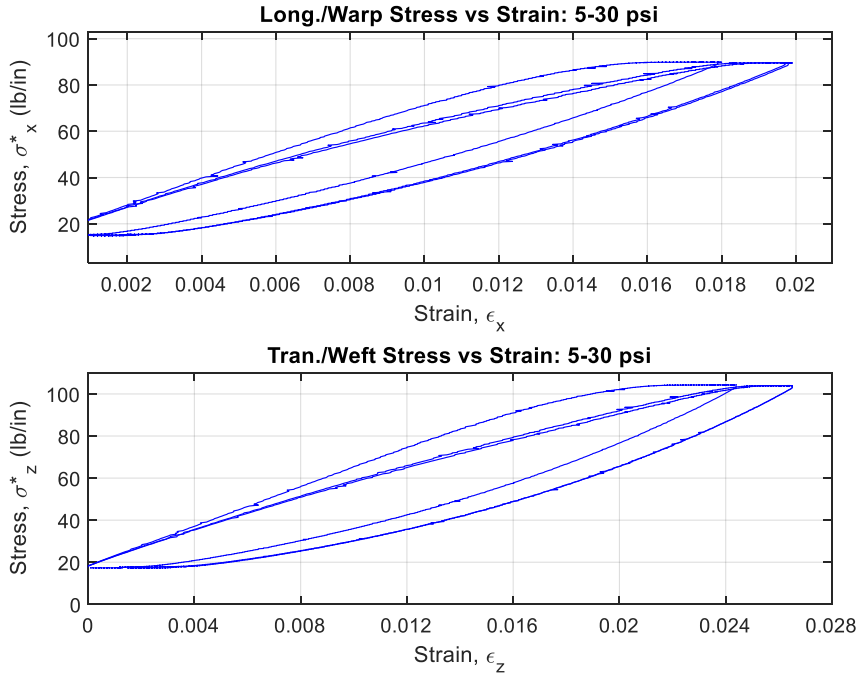

Figure 3.3: Stress vs Strain for 5-30 psi

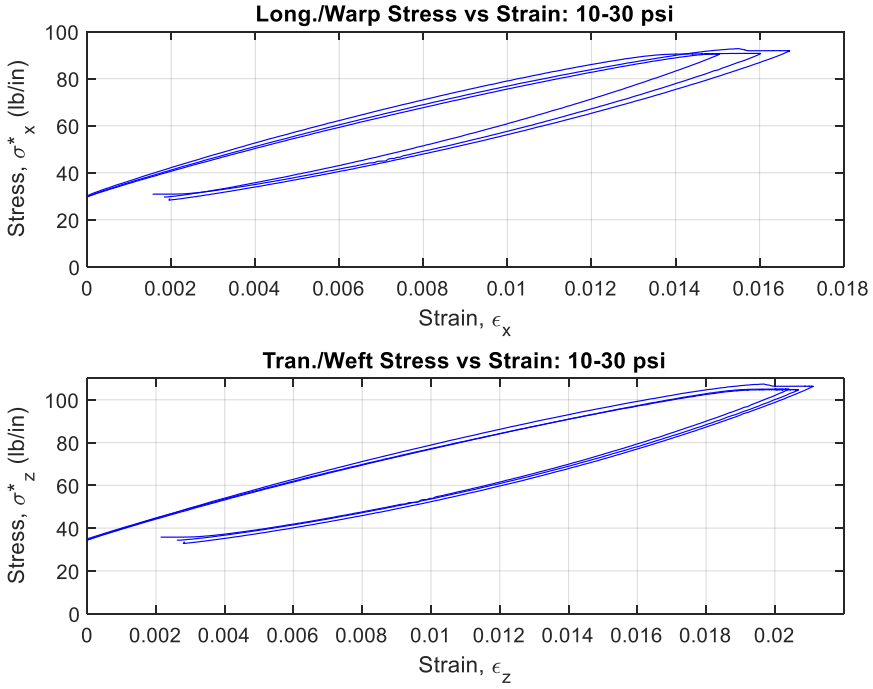

Figure 3.4: Stress vs Strain for 10-30 psi

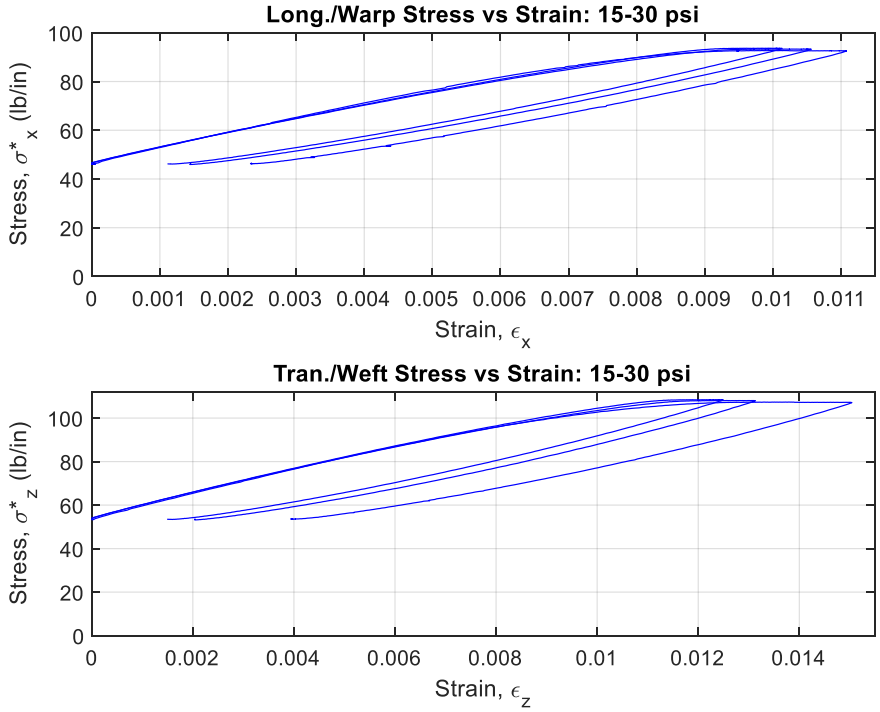

Figure 3.5: Stress vs Strain for 15-30 psi

Table 3.2: Computed Stresses and Strains for 5-30 psi Range

		@ 5 psi	@ 29.9 psi	Difference
Long./Warp Stress, σ_x^*		14.5 lb/in	86.8 lb/in	72.3 lb/in
Tran./Weft Stress, σ_z^*		17.4 lb/in	104 lb/in	86.4 lb/in
Test 1 Strains	**Long./Warp ε_x**	-1.28e-3	0.0139	0.0152
	Tran./Weft ε_z	-1.11e-3	0.0197	0.0208
Test 2 Strains	**Long./Warp ε_x**	-1.83e-3	0.0166	0.0184
	Tran./Weft ε_z	-1.65e-3	0.0238	0.0254
Test 3 Strains	**Long./Warp ε_x**	-1.92e-3	0.0172	0.0191
	Tran./Weft ε_z	-1.69e-3	0.0243	0.0260

Table 3.3: Computes Stresses and Strains for 10-30 psi Range

		@ 10 psi	@ 29.9 psi	Difference
Long./Warp Stress, σ_x^*		29.5 lb/in	88.3 lb/in	58.8 lb/in
Tran./Weft Stress, σ_z^*		35.4 lb/in	106 lb/in	70.6 lb/in
Test 1 Strains	**Long./Warp ε_x**	-1.08e-3	0.0131	0.0145
	Tran./Weft ε_z	-9.24e-4	0.0177	0.0186
Test 2 Strains	**Long./Warp ε_x**	-1.38e-3	0.0128	0.0142
	Tran./Weft ε_z	-1.35e-3	0.0189	0.0203
Test 3 Strains	**Long./Warp ε_x**	-1.22e-3	0.0138	0.0150
	Tran./Weft ε_z	-1.12e-3	0.0187	0.0199

Table 3.4: Computes Stresses and Strains for 15-30 psi Range

		@ 15 psi	@ 29.9 psi	Difference
Long./Warp Stress, σ_x^*		44.9 lb/in	89.4 lb/in	44.6 lb/in
Tran./Weft Stress, σ_z^*		53.8 lb/in	107.2 lb/in	53.4 lb/in
Test 1 Strains	**Long./Warp ε_x**	-9.05e-4	7.88e-3	8.78e-3
	Tran./Weft ε_z	-9.64e-4	0.0112	0.0121
Test 2 Strains	**Long./Warp ε_x**	-7.02e-4	8.02e-3	8.72e-3
	Tran./Weft ε_z	-5.24e-4	0.0107	0.0112
Test 3 Strains	**Long./Warp ε_x**	-6.12e-4	7.81e-3	8.42e-3
	Tran./Weft ε_z	-4.04e-4	0.0104	0.0176

From the coupon-level testing presented in Chapter 2, two Poisson's ratios were determined using a lower and upper range of loads. The lower range represents the stresses seen from inflation pressure only, resulting in a Poisson's ratio of $\nu_{xz} = 0.29$. Using Equation 3.5 and 3.6 and the values in Tables 3.2 through 3.4, the membrane moduli can be computed. Table 3.5 shows the membrane moduli for each test.

Table 3.5: Membrane Moduli (all units of lb/in)

		5 psi	10 psi	15 psi
Long./Warp Membrane Modulus, E_x^*	**Test 1**	3114	2697	3310
	Test 2	2560	2709	3336
	Test 3	2467	2558	3452
Tran./Weft Membrane Modulus, E_z^*	**Test 1**	3138	2829	3331
	Test 2	2572	2650	3543
	Test 3	2504	2657	3684

For the 5-30 psi, the first test produces significantly different moduli than the next two tests. Therefore, the average moduli are determined using test 2 and test 3. To ensure the moduli are comparable at other pressures, the average moduli is also taken for test 2 and test 3 for both the 10 psi and 15 psi. The average membrane moduli are listed below in Table 3.6.

Table 3.6: Average Membrane Moduli

	Long./Warp Membrane Modulus, E_x^* (lb/in)	**Tran./Weft Membrane Modulus, E_z^* (lb/in)**
5 psi	2514	2538
10 psi	2634	2654
15 psi	3394	3614

It can be observed that as the pressure increases, so do the membrane moduli. The longitudinal/warp membrane modulus for 10 psi is approximately 5% larger than the 5 psi membrane modulus, while at 15 psi the membrane modulus is 35% larger than at 5 psi. This shows that the pressure-dependency of the membrane moduli are non-linear. For the 5 and 10 psi, the longitudinal/warp modulus and the transverse/weft modulus are similar within 1%, while the transverse/weft modulus for 15 psi is 7% larger than the longitudinal/warp modulus for 15 psi. In all cases, however, the differences in the warp and weft direction are small, implying nearly isotropic behavior of the panel skin. This differs from the initial assumption that the panel has orthotropic behavior. It is important

to note that the equations derived for computing the stresses from Equations 2.4 and 2.5 are based on idealized cross-sectional geometry, which will slightly impact the computation of the membrane moduli. In prior research, tension tests of inflated woven fabric tubes for cylindrical inflated beams indicated a larger increase in the effective moduli with increasing pressure (Kabche et. al., 2011). These drop-stitch panels are made of a much heavier neoprene coating that will directly relate to the stiffness.

From the coupon-level testing in Chapter 2, the longitudinal/warp membrane modulus was estimated using uniaxial stresses. From the lower range specimens, the average modulus was 1843 lb/in. This value was computed over the last five load cycles producing fabric stresses corresponding to inflation pressure changes of 15 to 30 psi. In Table 3.6, the average longitudinal/warp membrane modulus for 15 psi is 3394 lb/in. The biaxial stress produces a more realistic modulus and is approximately 106% larger than the modulus computed from coupon-level testing. This large difference emphasizes the importance of accurately capturing the biaxial stress states when estimating skin moduli.

3.5 Torsion Test Design and Protocol

Torsion testing of the panel was conducted to calculate the membrane shear modulus for the panel skins, which must be known to estimate panel shear deflection. One end of the panel is clamped to a concrete block allowing for a fixed end. The other end of the panel is clamped to a frame attached to a shaft as seen in Figure 3.6. The shaft has a lever arm with a load cell and an actuator attached at its end via a steel cable. The actuator is electric and has a stroke of 18 in and a maximum load capacity of 1,000 lb. To determine the membrane shear modulus, three inclinometers are also attached to panel. The location

of these inclinometers can be seen in Figure 3.7. One inclinometer is attached to the lever arm to measure the inclination of the lever arm and allow the accurate calculation of applied torque. The other two inclinometers were attached directly on the panel at approximately 20% and 80% of the clamped length of the panel.

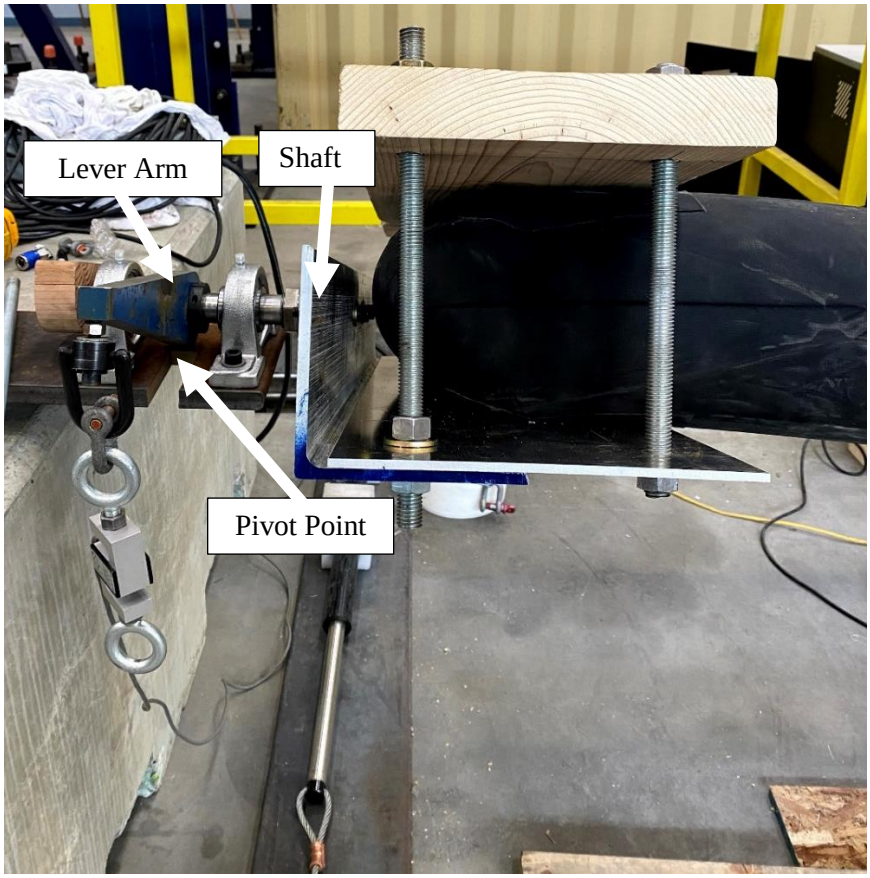

Figure 3.6: Clamped end of panel attached to a shaft

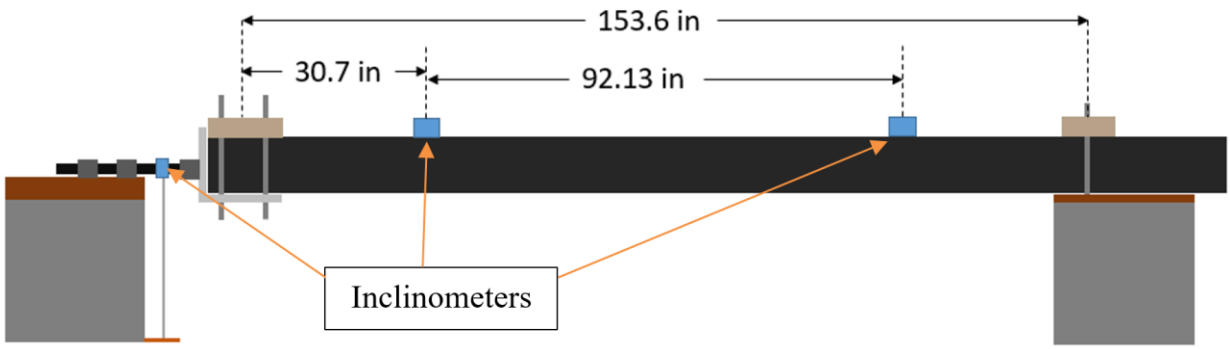

Figure 3.7: Inclinometer Locations on the panel

Figure 3.8 shows the initial twist in the panel. Due to this initial twist, the lever arm does not start at 0˚. To simplify the torque calculations, the actuator was positioned so that the cable was perpendicular to the floor at the start of each test. The actuator pulled down from a stationary point where the cable breaks around a pulley, and due to the rotation of the lever arm, the angle of the cable changed during the duration of the test. This will cause resultant forces at the end of the shaft in the z-direction (transverse) as well as the y-direction (vertical).

Figure 3.8: Starting Position of Panel for Torsion Testing

The panel was inflated to 5, 10 and 15 psi. For each pressure, the test was repeated three times, resulting in nine total tests. At the beginning of every test, the height of the pivot point on the hoist relative to the actuator plate was measured. Once the measurement was taken, the actuator was turned on and began to pull on the lever arm. The torque capacity of the keyless bushing on the shaft limited tests to a maximum load of 300 lb, and the actuator's maximum stroke was 18 in. Load was applied to the panel until either the load limit was reached, or the actuator reached is full stroke, whichever came first. The load was then released to a point where there was slack in the cable.

3.6 Calculation of Membrane Shear Modulus

To determine the torque applied on the panel an inclinometer was attached to the top of the lever arm and the actuator was located below the panel so that the initial pulling

is perpendicular to the floor. The lever arm is tapered, as shown in Figure 3.9, giving an offset of the recorded angle of 6.018 ˚. Attached to the lever arm is a hoist ring, and the pivot point of the hoist ring is 1.4375 in below the centerline of the lever arm. The length *d* from the pivot point to the end of the lever arm will always be perpendicular to the centerline of the lever arm. The height, g_i, from the ground to the pivot point on the hoist ring is recorded at the beginning of each test. A diagram of the lever arm can be seen below in Figure 3.9.

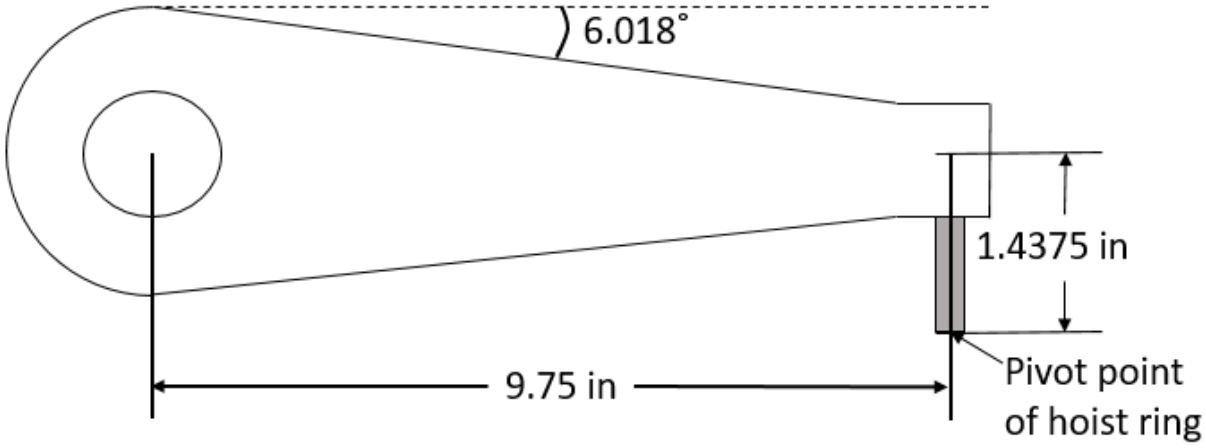

Figure 3.9: Dimensions of Torsion Lever Arm

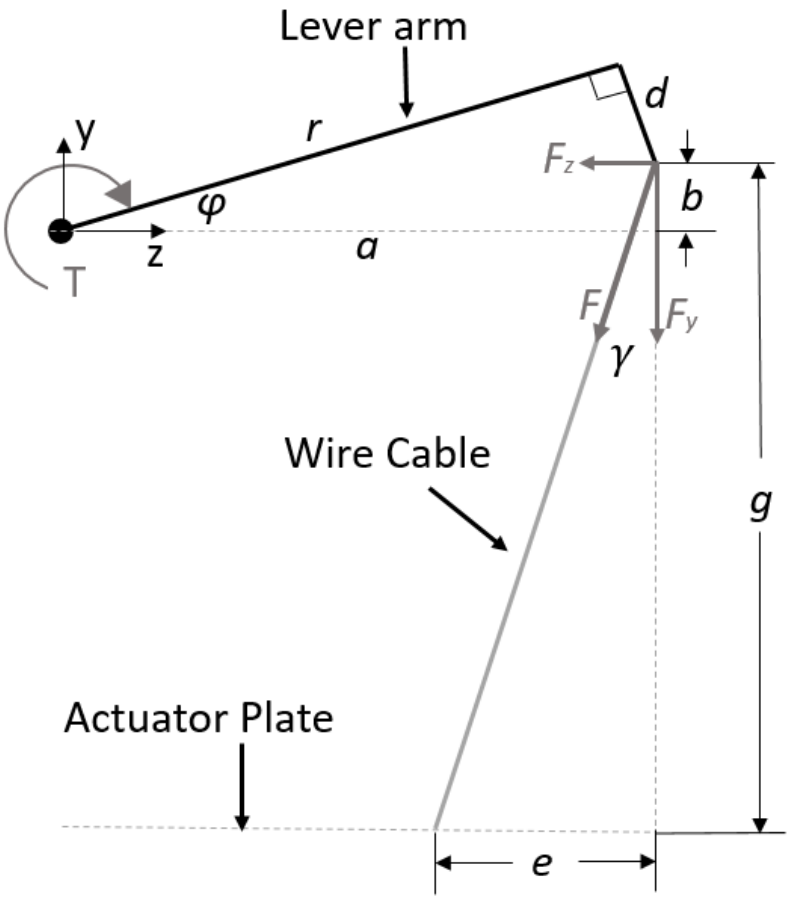

Figure 3.10: Geometry and Forces for Calculation of Applied Torque

Once the measured value of the inclinometer is offset from the taper, the reported value, φ, becomes the angle of the centerline of the lever arm to the horizontal as shown in Figure 3.10. The torque, T, obtained by taking the cross product of the position vector from the center of the shaft to the pivot point and the cable force F is defined in Equation 3.7.

$$T = a \cdot F_y - b \cdot F_z \tag{3.7}$$

Where F_y and F_z are the forces exerted by the cable at the pivot point in the negative y and negative z-directions, respectively. The values, a and b are the horizontal and vertical distances from the center of the shaft to the pivot point and depend on the angle φ as defined in Equations 3.8 and 3.9 below.

$$a = r \cdot \cos(\varphi) + d \cdot \sin(\varphi) \tag{3.8}$$

$$b = r \cdot \sin(\varphi) - d \cdot \cos(\varphi) \tag{3.9}$$

The radius, r, is the length of the lever arm from the center of the shaft to the hoist ring attachment point as seen in in Figure 3.9, and is a constant 9.75 in. The forces applied in the y- and z-direction are dependent on the angle of the cable γ as given in Equation 3.10, where g is the height to the pivot point and e is the horizontal distance from the pulley to the pivot point.

$$\gamma = tan^{-1}\left(\frac{e}{g}\right) \tag{3.10}$$

The values g and e vary as the actuator moves, therefore are defined as Equations 3.11 and 3.12.

$$g = g_i - \Delta b \tag{3.11}$$

$$e = a - a_i \tag{3.12}$$

Here g_i is the initial height to the pivot point and $\Delta b = b_i - b$ is the difference between the initial vertical distance, b_i, and the calculated b from Equation 3.9. In Equation 3.12, a_i is the initial length a when $\varphi = \varphi_i$. Therefore, $e = 0$ when $\varphi = \varphi_i$ due to the wire cable being perpendicular to the ground at the start of each test. The forces F_y and F_z exerted by the cable at the pivot point are obtained by resolving the cable force F reported by the load cell in Equations 3.13 and 3.14.

$$F_y = F\cos(\gamma) \tag{3.13}$$

$$F_z = F\sin(\gamma) \tag{3.14}$$

To determine the membrane shear modulus, we must first derive a relationship between the applied torque, T, and the angle of twist per unit length, θ. The angle of twist per unit

length for a thin walled closed section of uniform wall thickness is defined as (Equation 3.15)

$$\theta = \frac{T\ L_m}{4\ G^*\ A_m^2} \tag{3.15}$$

In Equation 3.15, A_m is the area enclosed by the median line, L_m is the length of the median line and G^* is the membrane shear modulus.

The torsion constant J^* is defined in Equation 3.16.

$$J^* = \frac{T}{G^*\ \theta} \tag{3.16}$$

Using Equations 3.15 and 3.16, calculation of the torsion constant can be simplified to Equation 3.17.

$$J^* = \frac{4\ A_m^2}{L_m} \tag{3.17}$$

The membrane shear modulus G^* can be determined using Equation 3.16 from the applied torque, T, and the angle of twist per unit length, θ, defined in Equation 3.18.

$$G^* = \frac{T}{J^*\ \theta} \tag{3.18}$$

The area enclosed by the median line, A_m, and the length of the median line, L_m, are shown below in Figure 3.11.

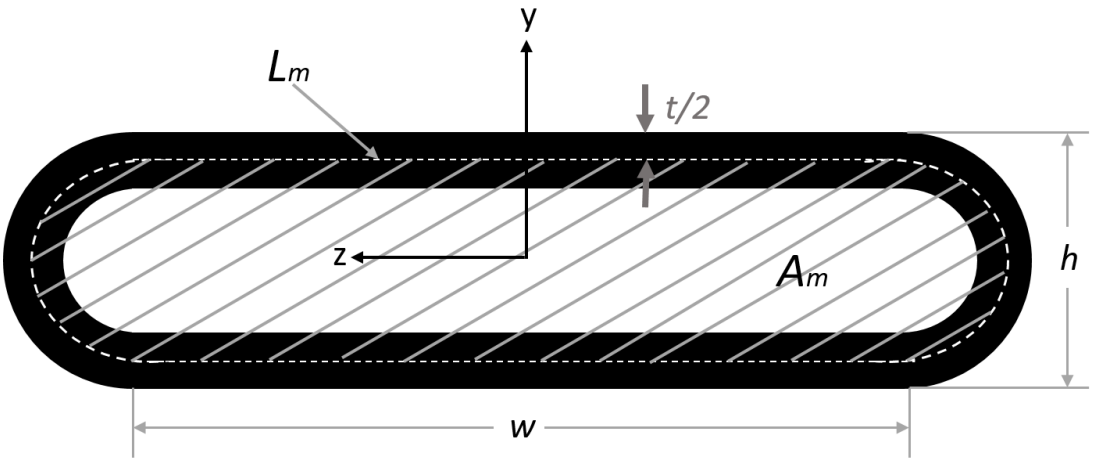

Figure 3.11: Cross-section area of DSP

The measured values of the panel are the height, h, and the effective width, w, and the outside perimeter, P, all reported in Chapter 2. Due to the actual thickness of the panel skins being small, the constitutive properties are all reported as membrane properties. For an accurate A_m and L_m, the thickness of the fabric is needed, however, and the thickness, t, was measured for the fabric used in the coupon testing. Assuming an idealized cross-section of two half circles and a rectangle, the measured perimeter is defined in Equation 3.19.

$$P = 2\,w + \pi\,h \tag{3.19}$$

The area enclosed and the length of the median line can be defined using measurable terms for the panel in Equations 3.20 and 3.21.

$$A_m = w(h - t) + \pi\left(\frac{h}{2} - \frac{t}{2}\right)^2 \tag{3.20}$$

$$L_m = 2\,w + \pi\,h - \pi\,t \tag{3.21}$$

Substituting Equation 3.19 into Equation 3.21 provides Equation 3.22 below.

$$L_m = P - \pi\, t \tag{3.22}$$

The calculated values for A_m, L_m and J^* are given below in Table 3.7 for all three pressures.

Table 3.7: Calculated Values for A_m, L_m and J^*

Variable	5 psi	10 psi	15 psi
A_m	190.9 in^2	196.9 in^2	201.5 in^2
L_m	65.02 in	65.34 in	65.57 in
J^*	2243 in^3	2373 in^3	2476 in^3

3.7 Torsion Testing Results

To obtain the angle of twist per unit length, θ, the angle of twist recorded between the two inclinometers mounted on the panel is divided by the distance between the two. This length is defined in Figure 3.7 as 92.13 in. To determine the torque per angle of twist per unit length (T/θ), a linear regression is used and the slope of that line is then divided by the calculated torsion constant J^* to determine the membrane shear modulus G^*. For the 10 psi and 15 psi test, the full loading curve is used to determine the slope. As seen in Figure 3.12, there is an anomaly at the highest loads at 5 psi, which may have been caused by the actuator reaching the end of its stroke. Due to this, only values up to 1400 lb-in were included in the linear regression at 5psi.

All results show initially stiffer response with some subsequent softening as more torque is applied, although the overall response is not highly nonlinear. For all pressures, the first test is offset from tests 2 and 3. This is expected due to the initial de-crimping of the fabric, and is typical for these panels when inflation tested and loaded in bending. The average membrane shear modulus for all pressures was therefore based on tests 2 and 3 at

each pressure. Figures 3.12 through 3.14 show the torque vs angle of twist for all tests run at 5 psi, 10 psi and 15 psi respectively.

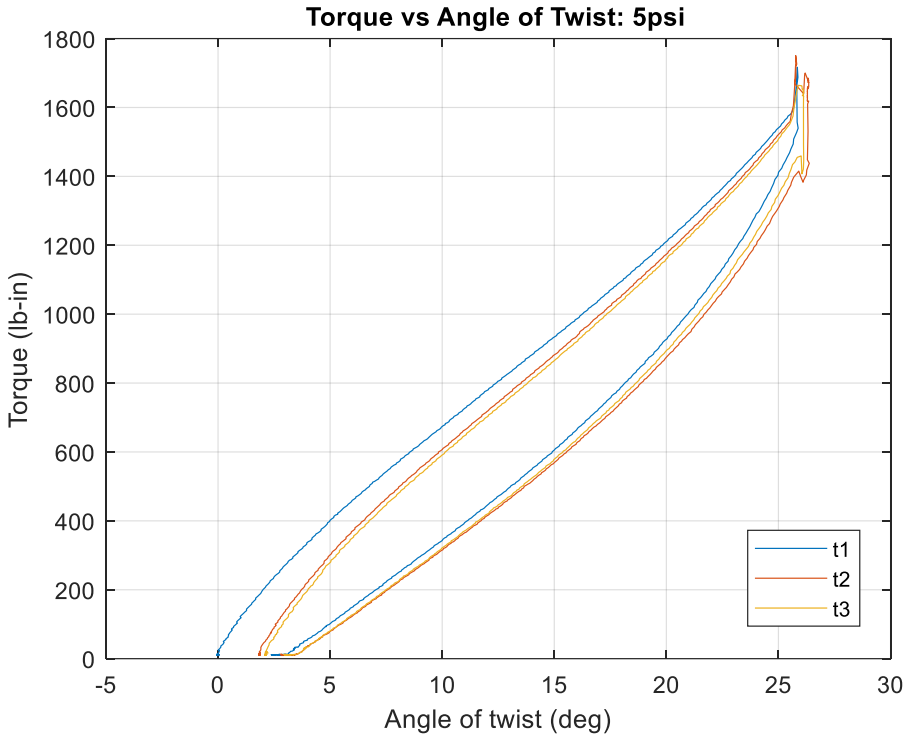

Figure 3.12: Torque vs Angle of Twist for 5 psi

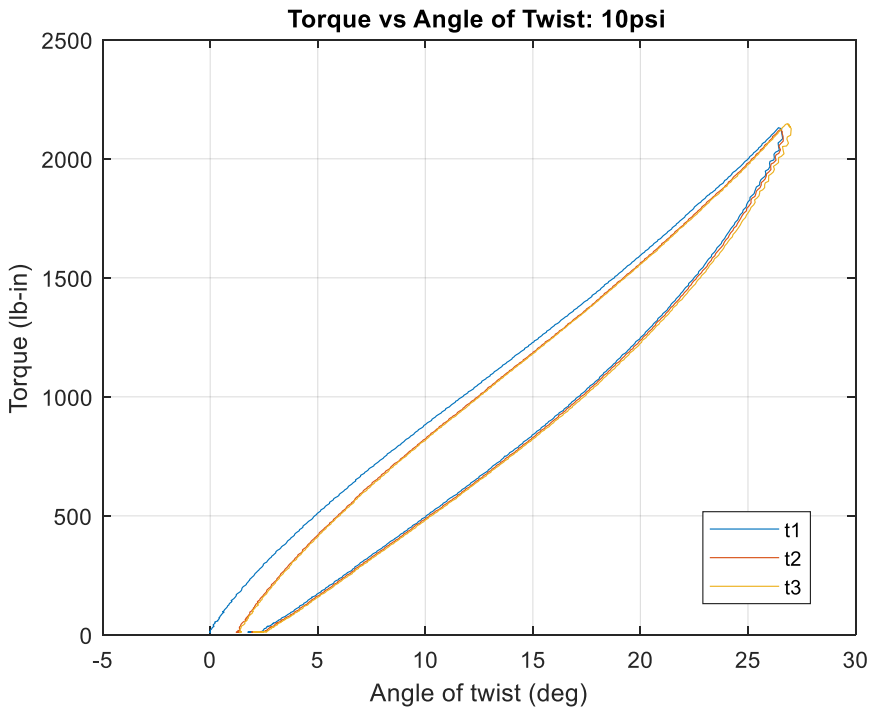

Figure 3.13: Torque vs Angle of Twist for 10 psi

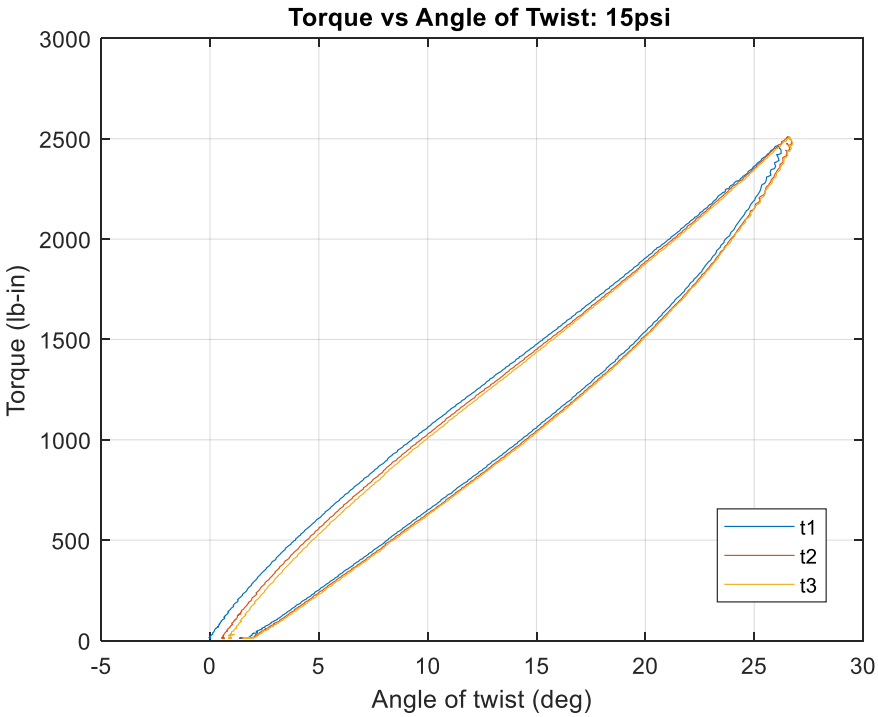

Figure 3.14: Torque vs Angle of Twist for 15 psi

Table 3.8 below lists the calculated membrane shear modulus for each test, including the average from tests 2 and 3. The membrane shear modulus at 15 psi is almost 40% larger than the membrane shear modulus at 5 psi. As observed in the inflation testing when determining the membrane moduli, E_x^* and E_z^*, drop-stitch inflatable panel membrane shear modulus also increases with inflation pressure. The moduli computed from the second and third tests at each pressure differ by at most 2% at the highest inflation pressure of 15 psi, and differences are even lower at 5 psi and 10 psi.

Table 3.8: Membrane Shear Modulus, G^* (lb/in)

Test	5 psi	10 psi	15 psi
1	137.2	173.8	196.7
2	146.9	181.2	201.1
3	147.0	181.0	205.2
Average	147.0	181.1	203.2

While both the membrane moduli and the membrane shear modulus are pressure-dependent, the shear modulus has a higher increase with inflation pressure than the membrane shear modulus. In prior research, torsion tests were conducted on inflated woven tubes used in airbeam construction, for approximately 10 psi to 20 psi, the membrane shear modulus increase by 30% (Kabche et. al, 2011). For these drop-stitch panels, from 5 to 15 psi, the increase was almost 40%.

Chapter 4

FOUR-POINT BEND TESTING

4.1 Introduction

The primary objective of this research is to develop testing procedures to determine the constitutive properties of orthotropic neoprene/nylon drop-stitch inflatable panel fabric and quantify panel load-deflection response on bending. While bending tests of drop-stitch panels have been reported, much of the work done on drop-stitch inflatable panels has focused on the determination of constitutive properties to help develop accurate modeling strategies and a better understanding of drop-stitch panel bending behavior. This chapter focuses on the determination of the load-deflection response of a drop stitch panel through four-point bend tests. The tests were conducted at different pressures and span lengths to assess the importance of these parameters. In addition, the constitutive properties determined in Chapters 2 and 3 are used in conjunction with Euler and Timoshenko beam theory to predict load-deflection response until the onset of wrinkling. The predictions are then compared with the experimental results to assess the quality of the constitutive properties and the appropriateness of Euler and Timoshenko beam theory for predicting response prior to wrinkling. .

4.2 Estimating the onset wrinkling and pre-wrinkling deflection of the panel using Euler Beam Theory

To determine the moment of inertia of the drop-stitch panel, the cross-section was idealized as two rectangles and two half-cylindrical shells. It must be noted that the actual panel geometry differs somewhat from this idealization: the panel edges consist of arcs

with included angles somewhat less than π and radii greater than half the panel depth. Using the parallel axis theorem, Equation 4.1 is found for I_z.

$$I_z = \frac{1}{12} \cdot w \cdot t^3 + w \cdot t \cdot \left(\frac{h}{2}\right)^2 + \frac{1}{12} \cdot w \cdot t^3 + w \cdot t \cdot \left(-\frac{h}{2}\right)^2 + \pi \cdot \left(\frac{h}{2}\right)^3 \cdot t \quad (4.1)$$

In Equation 4.1, w is the effective width of the panel, t is the thickness of the fabric, and h is the height of the panel. The moment of inertia calculated above has units of in^4. To get the moment of inertia and membrane modulus into similar terms, t is factored out of Equation 4.1, giving the membrane moment of inertia as Equation 4.2.

$$I_z{}^* = \frac{I_z}{t} = \frac{1}{12} \cdot w \cdot t^2 + w \cdot \left(\frac{h}{2}\right)^2 + \frac{1}{12} \cdot w \cdot t^2 + w \cdot \left(-\frac{h}{2}\right)^2 + \pi \cdot \left(\frac{h}{2}\right)^3 \quad (4.2)$$

The thickness of the panel is relatively small in comparison to the height of the panel; therefore, the first and third terms in Equation 4.2 are approximately zero. This gives the final equation of the membrane moment of inertia as Equation 4.3.

$$I_z{}^* = \frac{1}{2} \cdot w \cdot h^2 + \frac{1}{8} \cdot \pi \cdot h^3 \quad (4.3)$$

Membrane stress due to inflation pressure p, σ_x^*, was defined in Chapter 2 as Equation 4.4 below.

$$\sigma_x^* = \frac{p(wh + \pi h^2/4)}{2w + \pi h} \quad (4.4)$$

For a beam under bending, the stresses due to the internal bending moment are given by Equation 4.5.

$$\sigma_x^* = \frac{M \cdot y}{I_z{}^*} \quad (4.5)$$

Wrinkling of the panel will first occur on the top panel skin where $y = {}^{h}/_{2}$. The total membrane stress is the sum of the stress due to inflation pressure and the stress due to bending. Therefore, substituting Equation 4.3 and Equation 4.4 into Equation 4.5 and solving for the wrinkling moment M_w gives Equation 4.6.

$$M_w = \frac{p \cdot (w \cdot h + \pi \cdot \frac{h^2}{4})^2}{2 \cdot w + \pi \cdot h} \tag{4.6}$$

For a beam under four-point bending, the total applied force at wrinkling F_w is twice the wrinkling moment divided by the distance from the centerline of the support to the nearest load point, a. (Equation 4.7)

$$F_w = \frac{2 \cdot M_w}{a} \tag{4.7}$$

The estimated wrinkling load F_w can then be computed directly using Equation 4.8.

$$F_w = \frac{2}{a} \cdot \frac{p \cdot (w \cdot h + \pi \cdot \frac{h^2}{4})^2}{2 \cdot w + \pi \cdot h} \tag{4.8}$$

Using the measurements of the panel found in Chapter 2 and Equation 4.8, the wrinkling load for each internal pressure at each span length can be computed. These values can be seen below in Table 4.1.

Table 4.1: Estimated Wrinkling Load (units in inches)

Pressure (psi)	7 ft Span	10 ft Span	12 ft Span
5	197.9	138.6	115.5
10	434.4	304.1	253.4
15	645.9	452.2	376.8

Assuming Euler bending behavior, the deflection at the onset of panel wrinkling can be computed using Equation 4.9.

$$\delta_b = \frac{F_w \cdot a}{48 \cdot D} \cdot (3 \cdot L^2 - 4 \cdot a^2) \tag{4.9}$$

Here, δ_b is the deflection due to bending at wrinkling, L is the span length, and $D = E_x^* \cdot I_z^*$ is the bending rigidity. It is important to note that Equation 4.9 does not include shear deflections, so it is expected to over-estimate the panel stiffness to some extent.

From inflation testing, the longitudinal/warp membrane modulus E_x^* was found to be approximately 2514 lb/in for 5 psi, 2634 ln/in for 10 psi, and 3394 lb/in for 15 psi. Table 4.2 lists the values for the membrane moment of inertia I_z^*, the bending rigidity D, the wrinkling load F_w, and the estimated deflection due to bending, δ_b, at the wrinkling load for all pressures at each span.

Table 4.2: Computed Values for each pressure at different span lengths

Pressure, psi	**Span, ft**	I_z^*, **in^3**	D, **lb-in^2**	F_w, **lb**	δ_b, **in**
5	7	662	1.66e6	198	1.25
	10			138	2.55
	12			115	3.68
10	7	730	1.92e6	434	2.38
	10			304	4.85
	12			253	6.99
15	7	722	2.45e6	646	2.77
	10			452	5.66
	12			377	8.15

4.3 Deflection at wrinkling load including shear deformations with Timoshenko Beam Theory

To achieve a more accurate model for predicting deflection of the panel up until wrinkling, the Timoshenko beam theory can be utilized. Timoshenko beam theory has been used in previous studies for inflatable airbeams (Davids et. al, 2008). Timoshenko beam deformation takes into consideration the deformation due to both shear and bending. In Euler-Bernoulli beam theory, the plane sections remain plane and normal to the longitudinal axis, while in Timoshenko beam theory the plane sections do remain plane but are no longer normal to the longitudinal axis. The plane sections are rotated by a shear angle. Due to this, the transverse shear strain varies between the two load heads, but will remain constant through the cross-section. For the length of the beam that is between the end supports and the load heads, the shear force remains constant, therefore the shear strain also remains constant.

The slope of the deflection curve due to shear alone is approximately equal to the shear strain at the neutral axis of the beam. This is defined as Equation 4.10 below.

$$\frac{d\delta_s}{dx} = \frac{fV}{G^* A_v} \tag{4.10}$$

The form factor f is defined according to Timoshenko beam theory (Gere & Timoshenko, 1984). With the effective width of the panel being significantly larger than the thickness, $w \gg t$, it can be assumed that only the sidewalls carry significant shear stress. Also, with the assumption of an idealized cross-section, the form factor for a thin-walled tube can be applied, $f = 2$. The shear force, V, is defined as half the wrinkling load and A_v is the shear area. The shear area A_v is defined as $A_v = A_s/f$ and A_s is the area of the portion that resists

shear, in the case of the drop-stitch panels, this is assumed to be the sidewalls, therefore $A_s = \pi h$. Taking the integral of Equation 4.10 above, the deflection due to shear, δ_s, in four-point bending is defined as Equation 4.11.

$$\delta_s = \frac{F_w x}{2G^* A_v} \tag{4.11}$$

The deflection due to shear between the two load heads is zero due to the pure bending moment, but there is deflection due to shear up to the first load head, $x = L/3$, which is then added to the deflection due to bending at the mid-span.

In addition to the Timoshenko beam theory, Davids (2007), Davids et. al (2008) and Davids (2009) developed a theory that takes into consideration the pressure-volume work. The Timoshenko beam theory was used to quantify the effect of the pressure-volume work due to shear and bending. The pressure-volume work is proportional to the cross-sectional area enclosed by of the panel.. It is important to note that volume change due to shear deformation occurs at all levels of load including pre-wrinkling, while the volume change due to bending only occurs after wrinkling. Due to this, only the pressure-volume change due to shear deformations is taken into consideration, as all estimates are pre-wrinkling.

As shown in previous work (Davids et. al, 2008) (Davids, 2007), the pressure resultant P directly increases the effective shearing rigidity $G^* A_v$. The pressure resultant P is computed as the area enclosed by the panel skin multiplied by the internal pressure. Therefore, Equation 4.11 can be modified to include the pressure-volume change as Equation 4.12.

$$\delta_s = \frac{F_w x}{2(G^* A_v + P)} \tag{4.12}$$

Using the same estimated wrinkling load F_w from Equation 4.8, the deflections due to shear, bending and the total combined deflection at the wrinkling load can be seen in Table 4.3 for all three pressures at each span. The deflection due to bending δ_b, is determined at $x = L/2$, while the deflection due to shear is determined at $x = L/3$ because the deflection will not change between the load heads.

Table 4.3: Mid-Span Deflection at Estimated Wrinkling Load (inches)

		$\boldsymbol{\delta_b}$	$\boldsymbol{\delta_s}$	$\boldsymbol{\delta_{total}}$
7ft Span	5 psi	1.25	1.09	2.34
	10 psi	2.38	1.46	3.85
	15 psi	2.77	1.70	4.48
10ft Span	5 psi	2.55	1.09	3.64
	10 psi	4.86	1.47	6.33
	15 psi	5.66	1.71	7.37
12ft Span	5 psi	3.67	1.09	4.76
	10 psi	6.99	1.47	8.46
	15 psi	8.14	1.71	9.85

For the estimated deflection response at the load heads, the deflection due to shear remains the same, but the deflection due to bending at $x = L/3$ is estimated as Equation 4.13.

$$\delta_{b\_lh} = \frac{F_w L}{36D}(L^2 - \frac{L^2}{3} - \frac{L^2}{9}) \tag{4.13}$$

Table 4.4 below shows the estimated deflection at the load heads at the estimated wrinkling load for all spans and pressures.

Table 4.4: Load Head Deflection at Estimated Wrinkling Load (inches)

		δ_b	δ_s	δ_{total}
7ft Span	5 psi	1.09	1.09	2.18
	10 psi	2.07	1.46	3.54
	15 psi	2.41	1.70	4.12
10ft Span	5 psi	2.22	1.09	3.31
	10 psi	4.23	1.47	5.69
	15 psi	4.92	1.71	6.63
12ft Span	5 psi	3.19	1.09	4.28
	10 psi	6.08	1.47	7.55
	15 psi	7.08	1.71	7.08

4.4 Bend Test Protocol

The four-point bend test setup allows the panel to be tested without the use of a large frame. The panel is clamped between two wheel supports to allow the panel ends to move freely in the horizontal direction and rotate freely. As shown in Figure 4.1 below, the center of the wheels are near the mid-height of the panel. While the height of the panel varies slightly with pressure, the wheels are set at a constant 3.5 inches from the bottom of the panel.

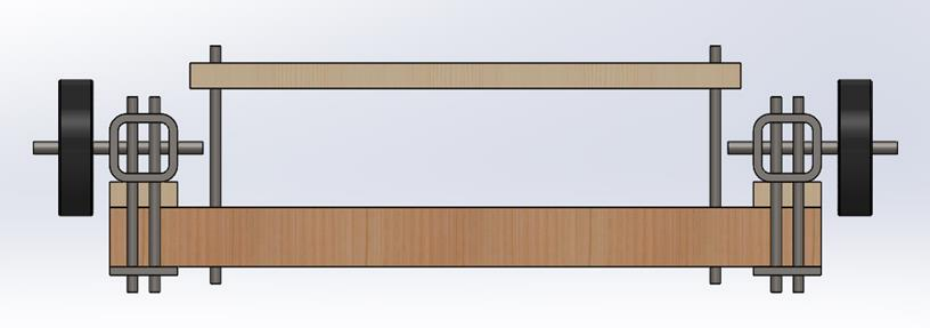

Figure 4.1: Bend Test Wheel Supports

A load assembly is placed on top of the panel with four straps and a spreader bar, and an 18-inch stroke electric actuator then pulls down the panel. This is the same actuator used in the torsion testing to determine the membrane shear modulus. The load assembly, straps and wheels are all adjustable for each span being tested. For the load assembly seen

in Figure 4.2 the two 4x4s on top are the load heads resting on the panel. The load heads each have PTFE sheets on the bottom and are curved to reduce stress concentrations and minimize restraint of the panel. The 2x4s connecting the load heads are connected to the 4x4s via the eyebolts and different length 2x4s can be easily installed to produce different load spans. From center to center of the load heads, the distance is always 1/3 of the span length. The straps are adjustable to make sure the spreader bar is always the same height. The load cell at the bottom of Figure 4.2 records all the load being pulled by the actuator, but does not include the weight above the load cell. To account for this, the weight of the load assembly is measured before testing and added to the recorded actuator load.

Figure 4.2: Load Assembly

Seven string potentiometers were used to record the displacement of the panel. Two were attached to the spreader bar from the ground, and five attached to the centerline of the panel. A front view of the panel can be seen in Figure 4.3, and a drawing of the panel with

measurements for a 7 ft span, 10 ft span, and 12 ft span can be seen in Figures 4.4 through 4.6.

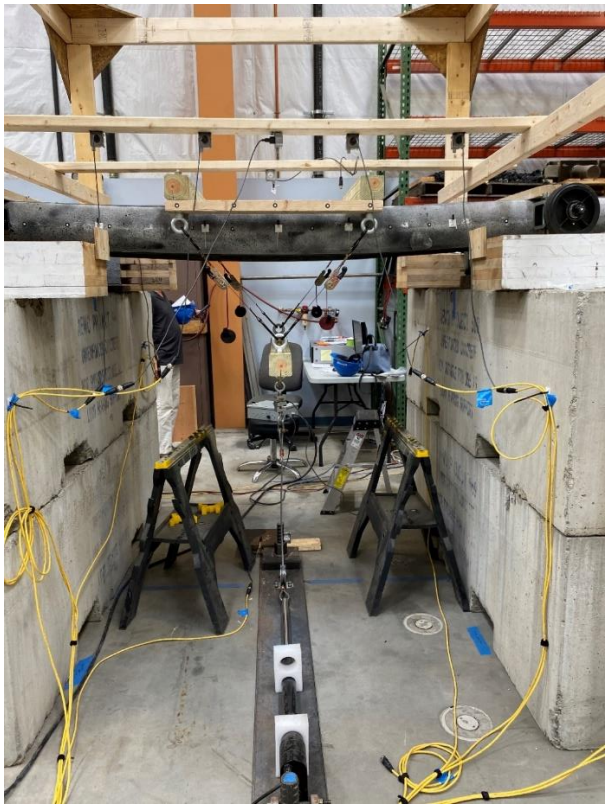

Figure 4.3: Panel K459A Initial Testing, 7 ft Span

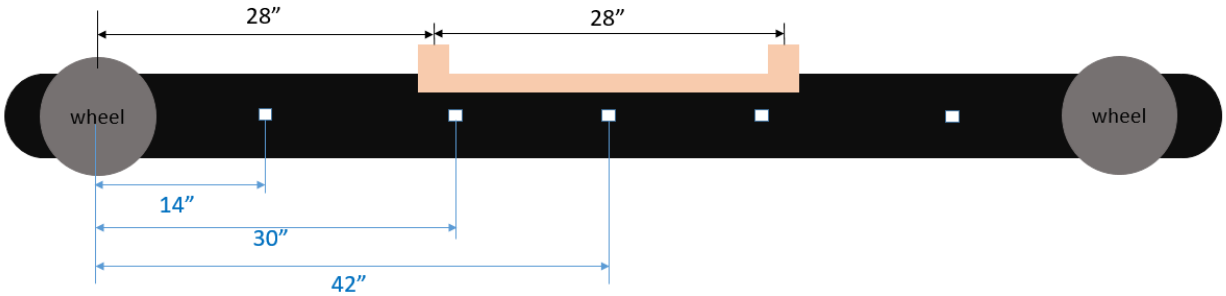

Figure 4.4: String Potentiometers for 7 ft Span

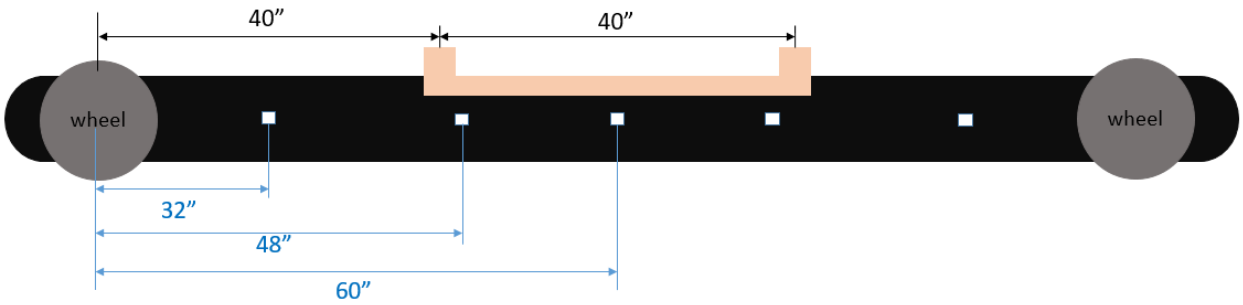

Figure 4.5: String Potentiometers for 10 ft Span

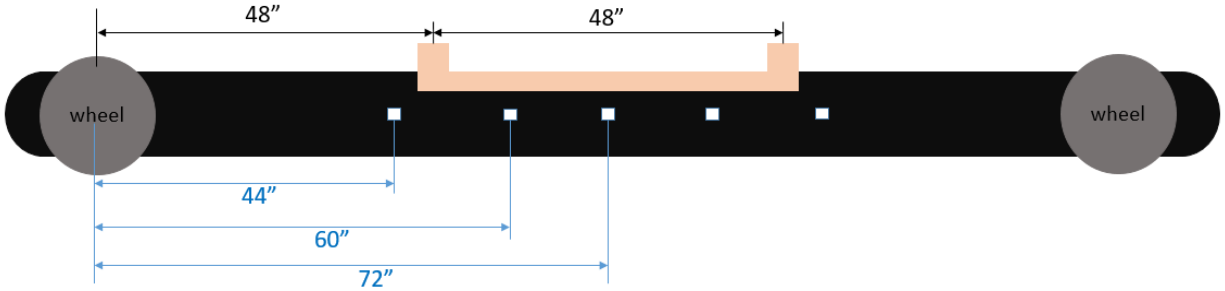

Figure 4.6: String Potentiometers for 12 ft Span

Due to the initial twist in the panel as discussed in Chapter 2 and shown in Figures 2.2 through 2.7, the panel was only tested for 5, 10, and 15 psi. For each pressure, the actuator was run at half and full speed, which corresponded to test times of approximately 90 secs and 45 secs from the point at which the actuator began to load the panel until the target maximum displacement of ~10 in was reached. This was done to determine if the load rate affects the results of the panel deformations.

Before running each test, the initial curved shape of the panel was measured by taking the distance from a taut string attached at the center of the wheel supports to the top of the panel as illustrated in Figures 4.7 through 4.9. The string is attached to the center of the 2x4 clamping the panel at the wheels and is touching the top of the 2x4 as well. This means at the center of the wheels, the string is 1.5 inches above the top of the panel. Tables

4.5 through 4.7 show the average measurement from the string to the top of the panel at the three inflation pressures.

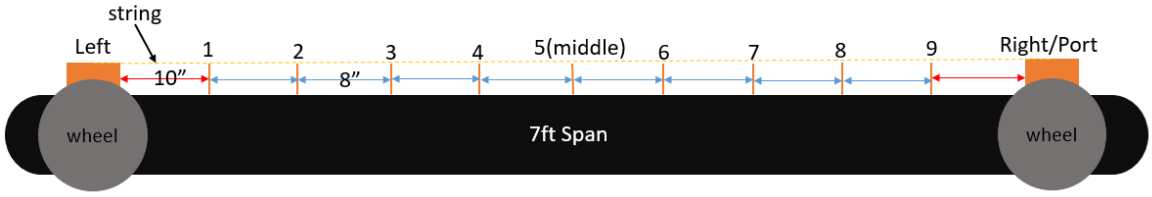

Figure 4.7: Initial Measurements for 7 ft Span

Table 4.5: Average measurements from the string to the top of panel for a 7 ft span (all units in inches)

	1	2	3	4	5	6	7	8	9
5 psi	2.094	2.427	2.719	2.865	2.979	2.979	2.760	2.479	2.104
10 psi	2.115	2.417	2.656	2.781	2.854	2.844	2.688	2.417	2.083
15 psi	2.086	2.325	2.516	2.602	2.664	2.641	2.500	2.305	2.047

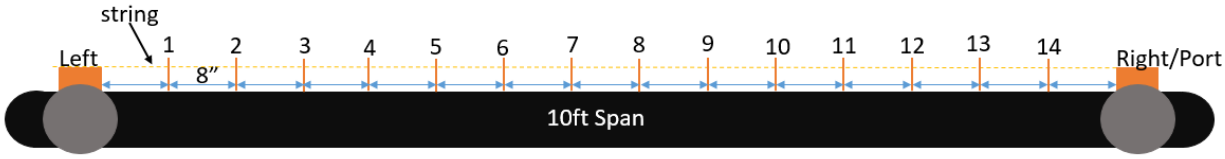

Figure 4.8: Initial Measurements for 10 ft Span

Table 4.6: Average measurements from the string to the top of panel for a 10 ft span (all units in inches)

	1	2	3	4	5	6	7	8	9	10	11	12	13	14
5 psi	2.38	2.99	3.57	3.98	4.33	4.59	4.69	4.69	4.48	4.25	3.85	3.34	2.83	2.09
10 psi	2.31	2.85	3.30	3.65	3.93	4.12	4.20	4.20	4.05	3.86	3.58	3.15	2.74	2.15
15 psi	2.34	2.88	3.34	3.64	3.91	4.10	4.24	4.21	4.05	3.92	3.66	3.22	2.81	2.24

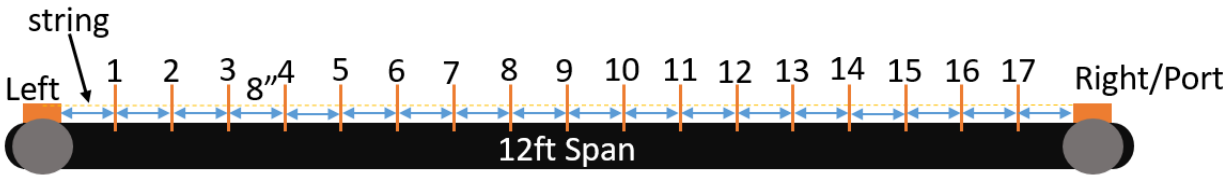

Figure 4.9: Initial Measurements for 12 ft Span

Table 4.7: Average measurements from the string to the top of panel for a 12 ft span (all units in inches)

	1	2	3	4	5	6	7	8	9
5 psi	2.77	3.59	4.36	5.08	5.62	6.03	6.38	6.55	6.55
10 psi	2.57	3.23	3.84	4.38	4.82	5.17	5.44	5.56	5.56
15 psi	2.60	3.29	3.88	4.45	4.86	5.15	5.35	5.57	5.59
	10	**11**	**12**	**13**	**14**	**15**	**16**	**17**	
5 psi	6.37	6.15	5.78	5.24	4.57	3.79	2.95	2.13	
10 psi	5.44	5.22	4.93	4.56	4.00	3.37	2.73	2.08	
15 psi	5.46	5.25	4.98	4.59	4.10	3.45	2.82	2.17	

Before recording any data with the MTS system, the center-to-center measurement between the wheel supports was also taken. Once all these initial measurements were taken, MTS data acquisition is turned on, running at 10.24 Hz, and the data from the pressure transducer, load cell, and string potentiometers begin to record. The load assembly is then put on top of the panel, with the straps and the spreader bar with the attached load cell. This allows the displacement of the panel caused by the weight of the load assembly to be measured. The total weight of the apparatus for a 7 ft span above the load cell (which includes the load assembly, straps, spreader bar, and shackles) was 40.32 lb. The last instrumentation to be attached to the set-up is the string potentiometer that is on the ground attached to the spreader bar. Load apparatus weights for each test span are given in Table 4.8.

Table 4.8: Weight of Load Apparatus

Span (ft)	Weight (lb)
7	40.32
10	42.14
12	49.27

The actuator is then set at a desired speed and the panel is deflected approximately 10 inches and is then unloaded without pausing. The test is stopped, data is exported, and everything is reset to run the next test.

4.5 Bend Test Results

Exported data include a time stamp, load, pressure, and displacements at each string potentiometer. All string potentiometers are zeroed and the load is offset to take the weight of the load assembly into consideration. The data collected from the MTS system are the displacements of the string potentiometers, the internal pressure of the panel and the load from the load cell. Data acquisition begins right before the load assembly is placed on top of the panel. The weight of the entire load apparatus is known (Table 4.8) and used later is the process. The data is then imported into a MatLAB code and the load is adjusted to include all weight from the load apparatus not recorded by the load cell, which hangs below. The stage where peak deflection occurs is determined, as well as what stage the actuator begins pulling on the panel. The maximum deflection from the string potentiometer at the mid-span is utilized as it is where the maximum panel deflection would occur. To determine the stage where the actuator begins to pull on the panel, the code works backwards from the stage of peak deflection until the deflections of the previous stage is equal to the current stage. Once this start stage is known, all string potentiometers are zeroed.

Due to the initial curve in the panel as well as the weight of the load assembly, as seen in Figure 4.10, the data does not pass through the origin. To account for these initial conditions, an offset is determined to pass the data through the origin. This is done using a linear regression. To be consistent through all pressure and span lengths, the data used for the linear regression is everything before approximately 75% of the estimated wrinkling load within ±5 lb.

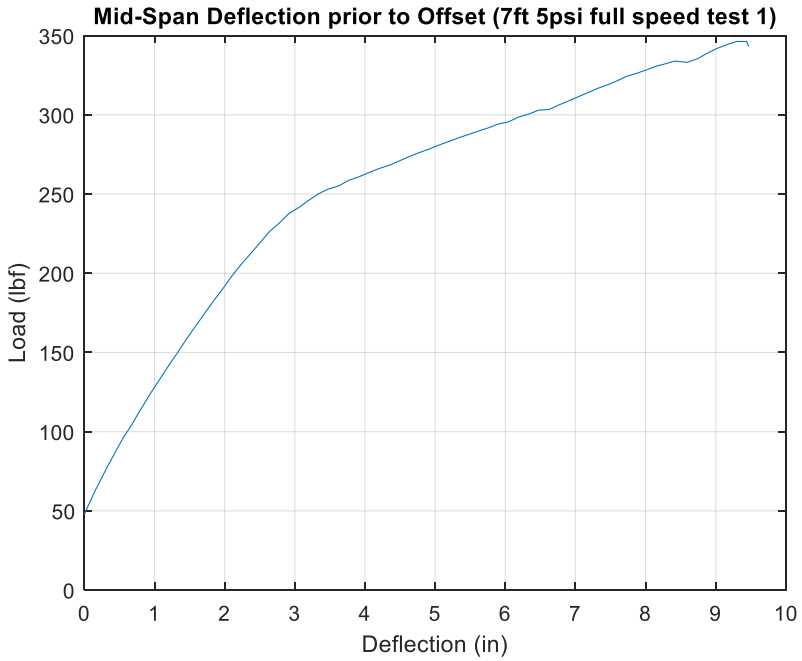

Figure 4.10: Mid-Span Deflection prior to Offset

Figures 4.11 through 4.19 below show the results from all span lengths and pressures at the mid-span the load-heads. These figures include full (solid) and half load (dashed) rates, showing there is only an insignificant difference between the load rates. Figures 4.11 through 4.13 show the applied load versus the deflection for a 7 ft span at 5, 10 and 15 psi respectively. Figures 4.14 through 4.16 show the applied load versus deflection for a 10 ft for all three pressures, and Figure 4.17 through 4.19 show the applied

load versus deflections for 12 ft span. The circle on the graphs represents the estimated deflection using Euler-Bernoulli beam theory, while the x on the graph is for the estimated deflection using a straightforward application of linearly elastic Timoshenko Beam theory, both are at the wrinkling load.

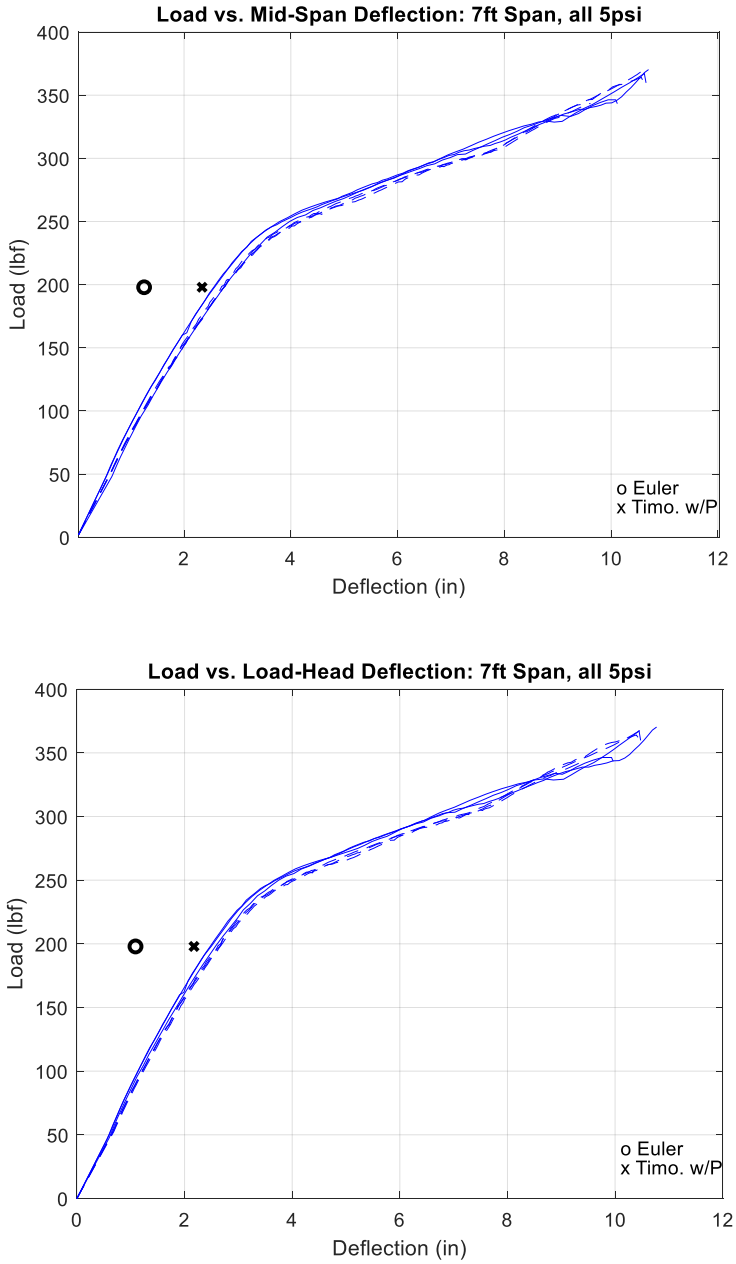

Figure 4.11: Load vs Mid-Span Deflection: 7ft Span, all 5 psi

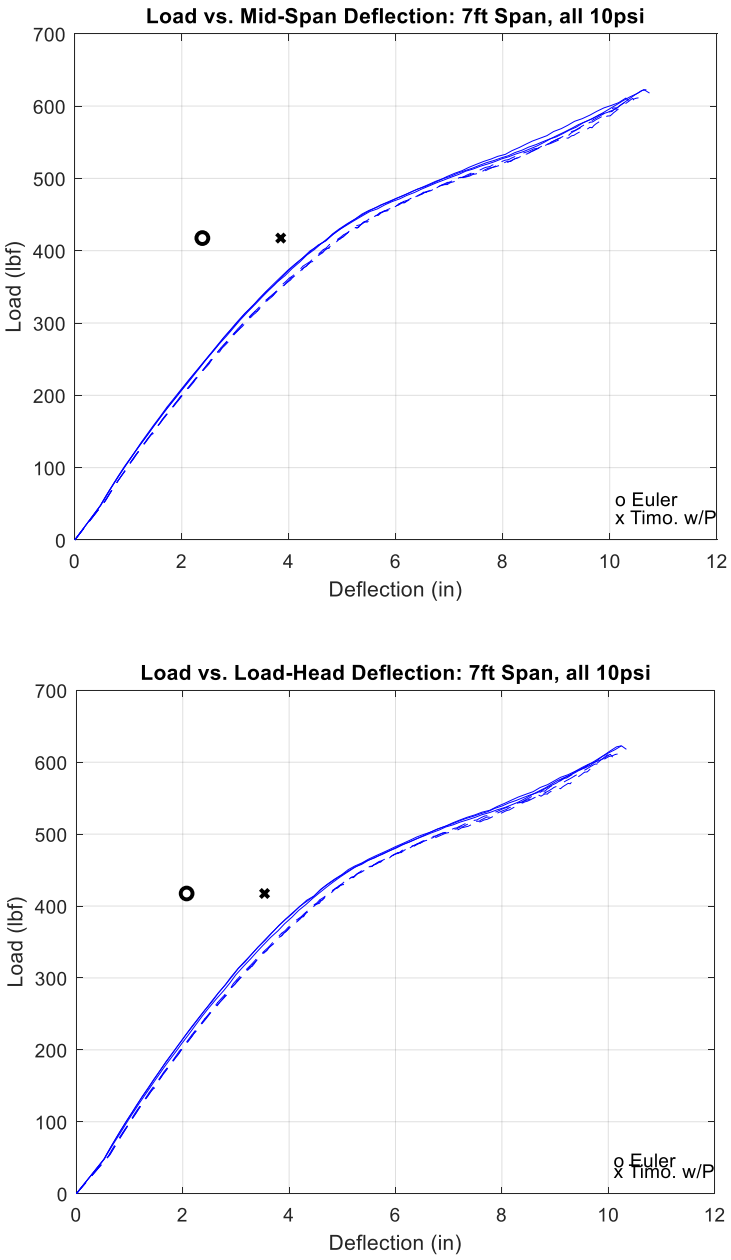

Figure 4.12: Load vs Mid-Span Deflection: 7 ft Span, all 10 psi

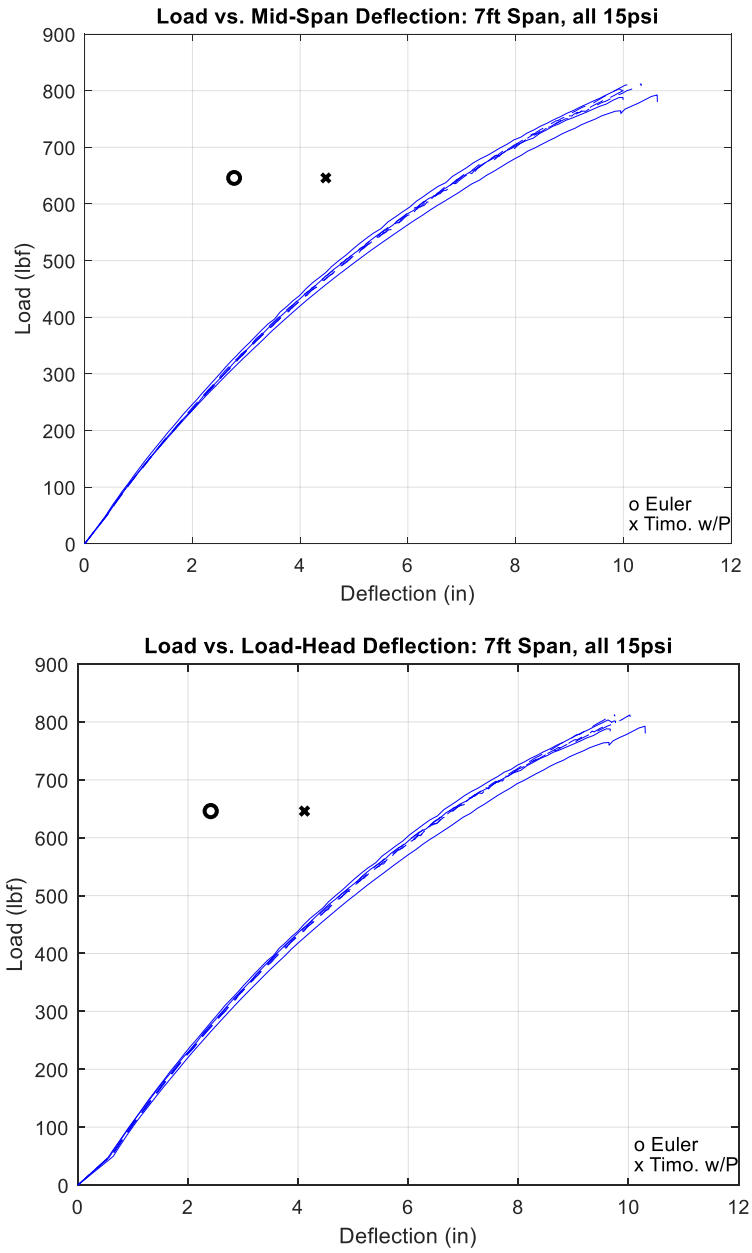

Figure 4.13: Load vs Mid-Span Deflection: 7 ft Span, all 15 psi

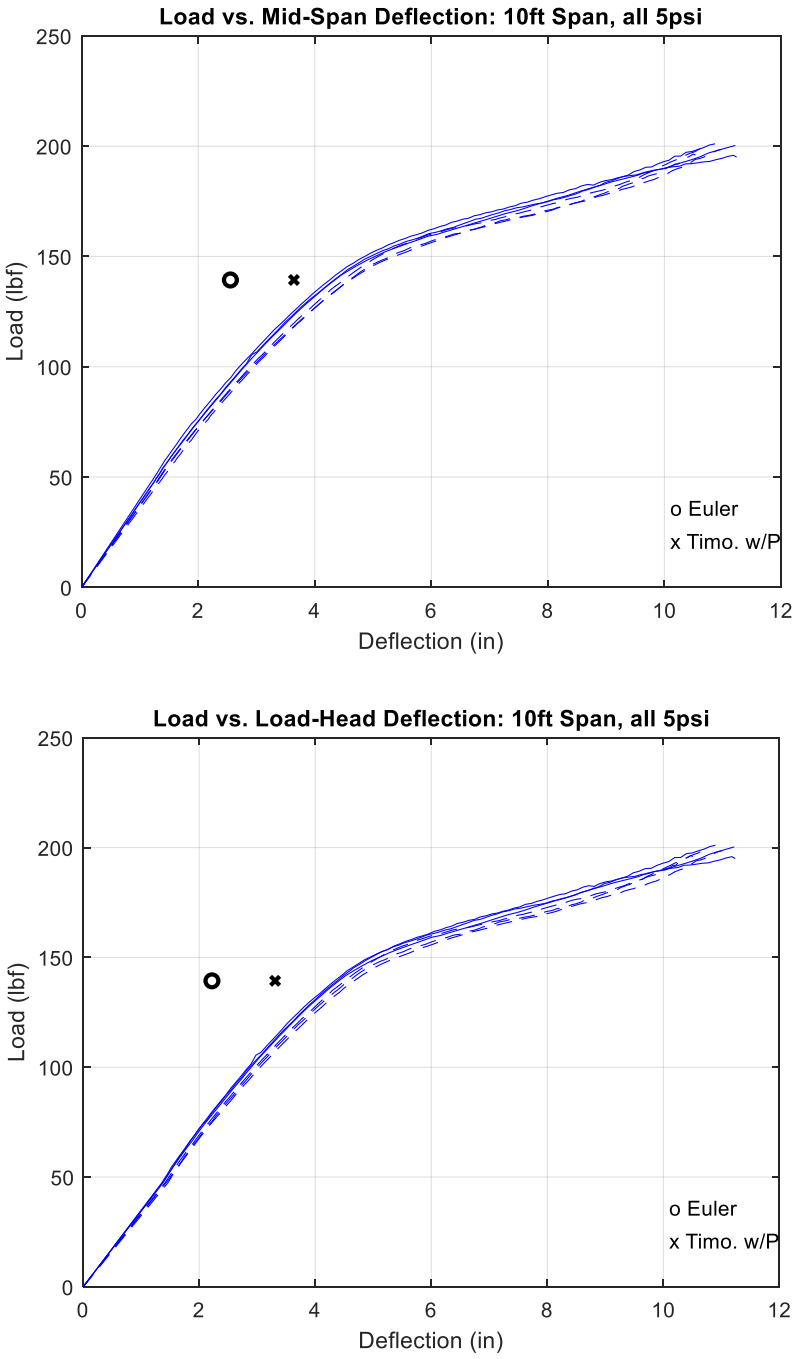

Figure 4.14: Load vs Mid-Span Deflection: 10 ft Span, all 5 psi

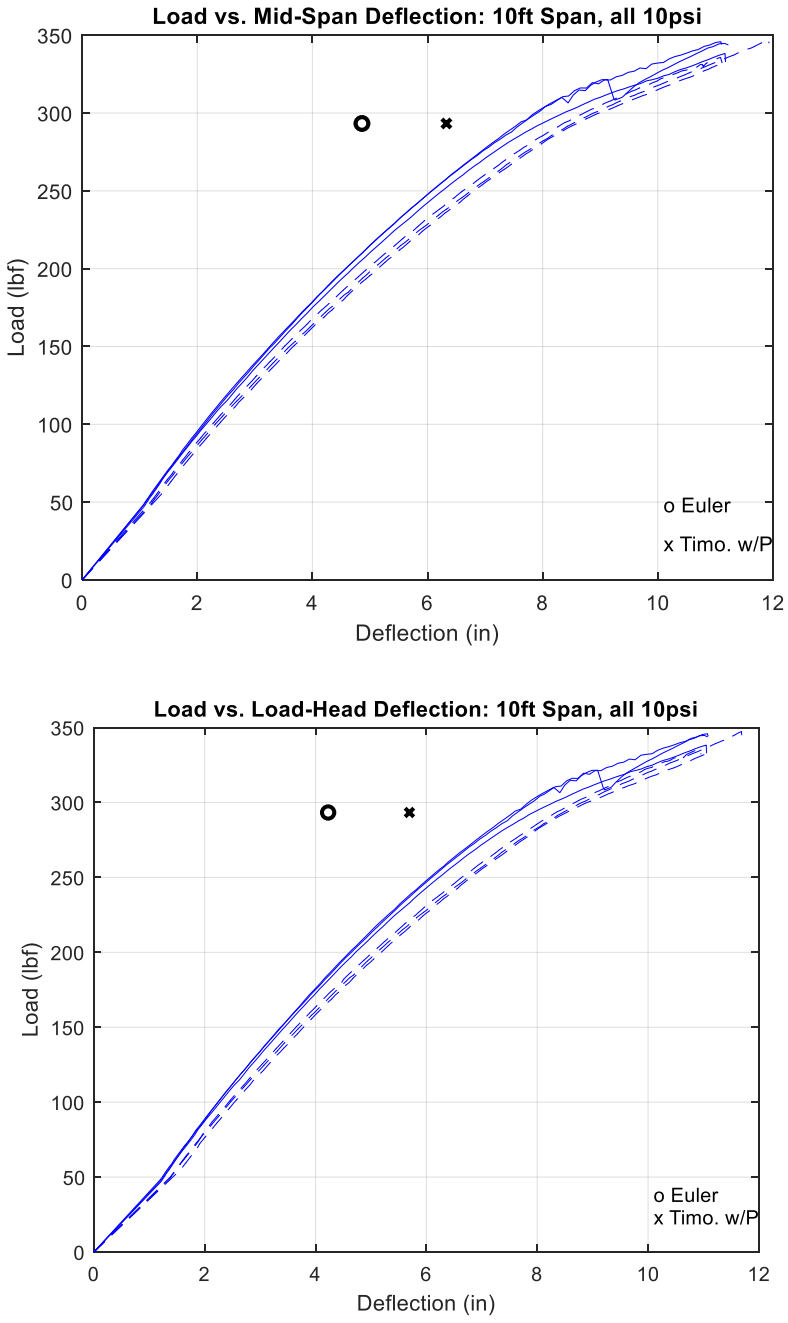

Figure 4.15: Load vs Mid-Span Deflection: 10 ft Span, all 10 psi

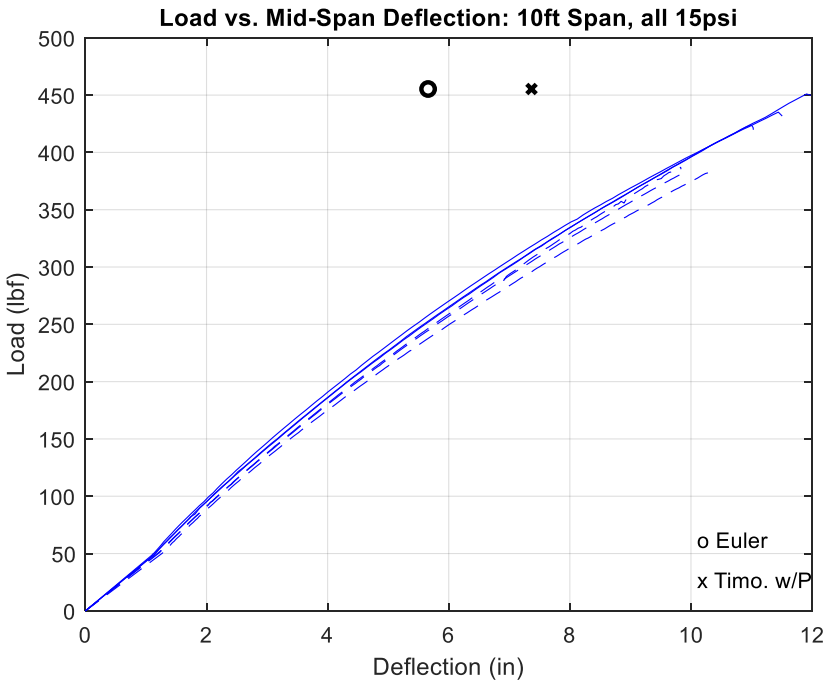

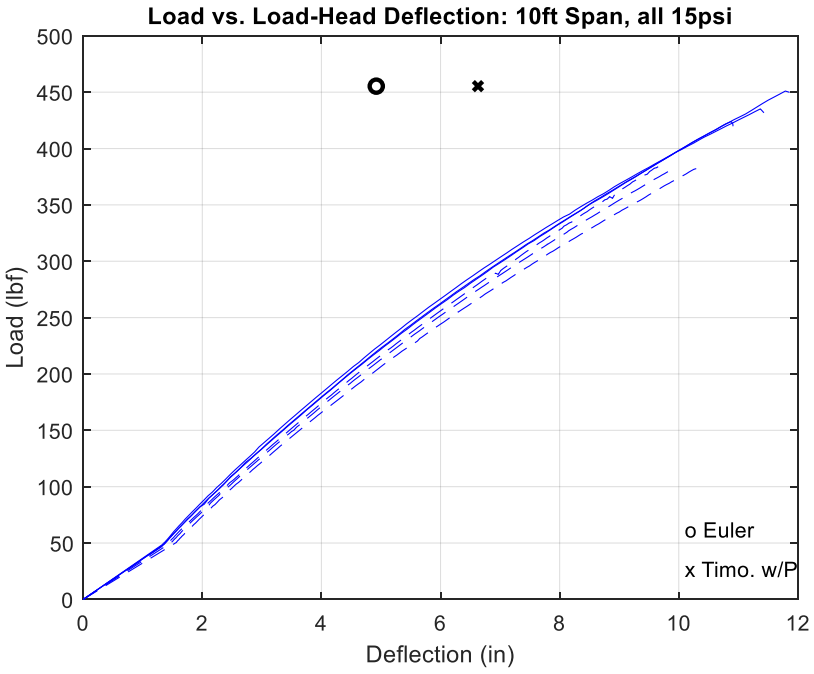

Figure 4.16: Load vs Mid-Span Deflection: 10 ft Span, all 15 psi

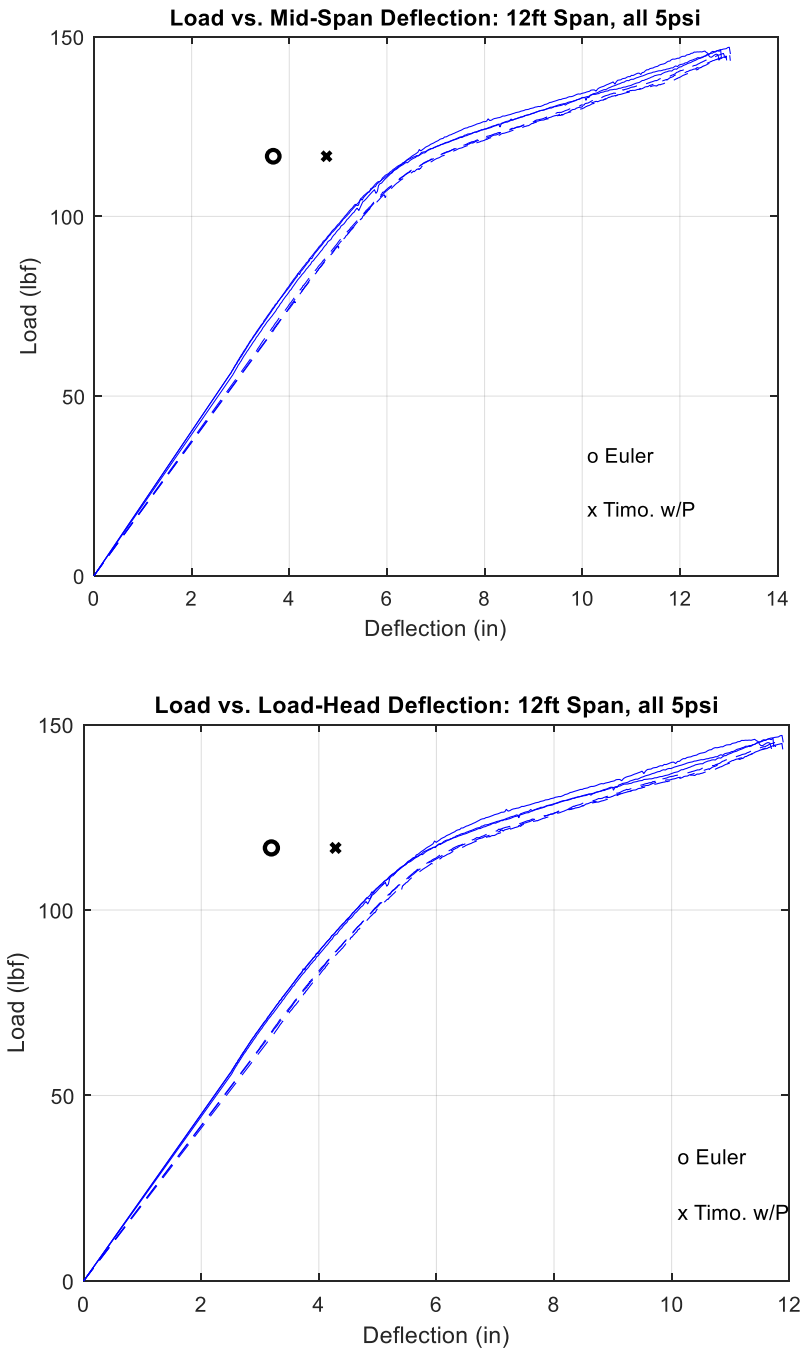

Figure 4.17: Load vs Mid-Span Deflection: 12 ft Span, all 5 psi

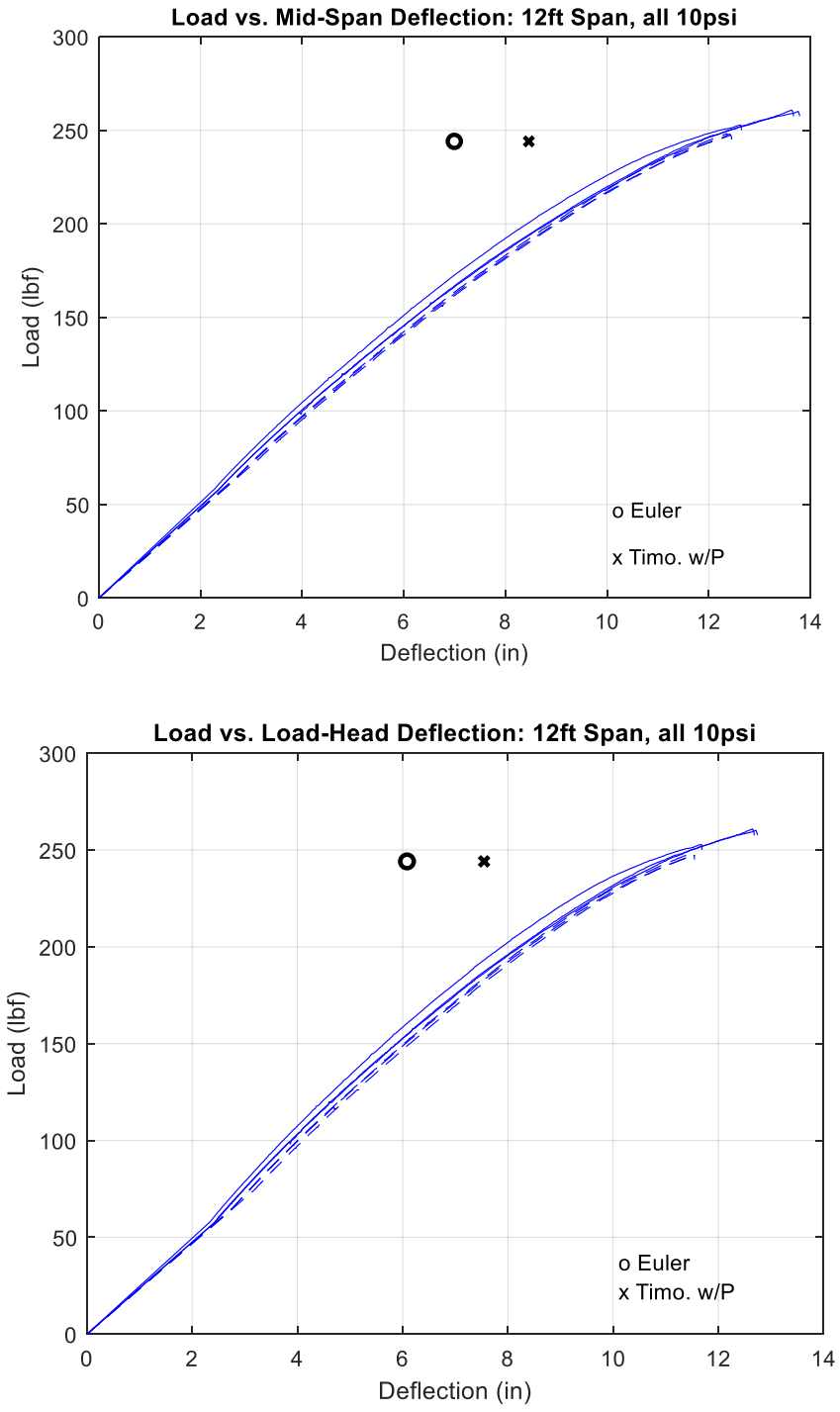

Figure 4.18: Load vs Mid-Span Deflection: 12 ft Span, all 10 psi

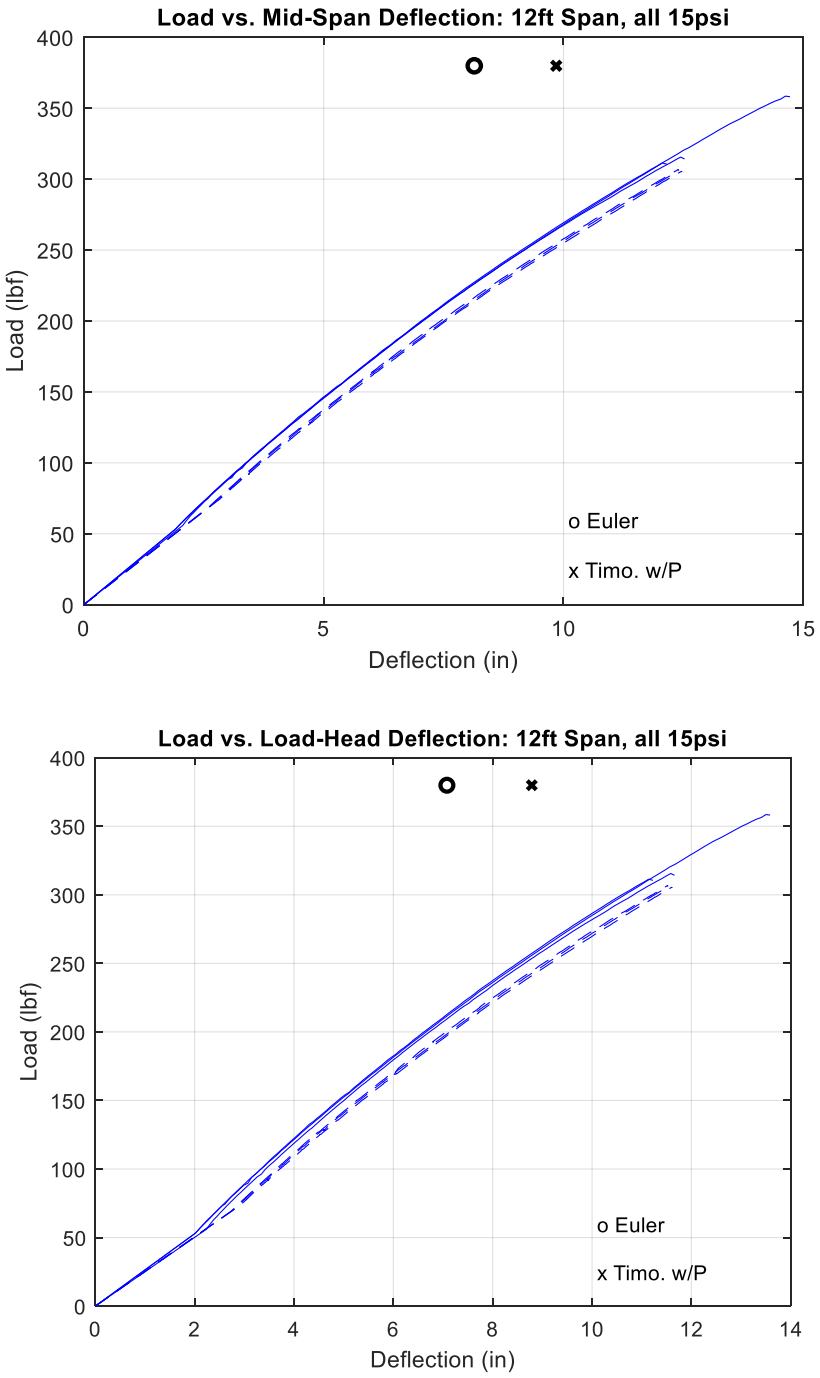

Figure 4.19: Load vs Mid-Span Deflection: 12 ft Span, all 15 psi

There was more wrinkling observed in the 7 ft span tests than the 12 ft spans. This is due to the 12 ft span being more flexible. The actuator was limited by the stroke, therefore at

the higher span the test did not get as far past the wrinkling load as what was observed in the 7 ft spans.

As observed for all testing above, using Euler-Bernoulli beam theory for estimating the deflection at the wrinkling load is not an accurate form of modeling for drop-stitch inflatable panels, and a stiffer response is consistently predicted. However, the predicted wrinkling load corresponded reasonably well with the onset of observed nonlinear load-deflection response, especially at lower inflation pressures and shorter spans where more wrinkling occurs. Using a straightforward application of linearly elastic Timoshenko beam theory and pressure volume work developed in Davids et al (2008), the response is also predicted to have a stiffer response that the experimental data for the majority of tests. This Timoshenko deflection estimation with pressure-volume work is closer however to the experimental response of the panel. For all estimations of deflections, an idealized cross-section of two half-circle and a rectangle with orthotropic elasticity were used. As mentioned is Chapter 3 when discussing the experimental results of the inflation testing, the differences in the warp and weft direction are small, implying nearly isotropic behavior of the panel skin. Therefore, the assumption of orthotropic elasticity for a rubber coated fabric may not be necessary. It is also important to note that while both the Euler-Bernoulli and Timoshenko beam theories both predicted stiffer than measured responses, the Timoshenko estimate being closer to the experimental response emphasizes the importance of including shear deformations in models for drop-stitch panels.

As expected, when the pressure increases the stiffness of the panel also increases. This was shown in the inflation testing results for the membrane moduli, the bend testing supported this. It was also expected that the deflection would increase as the span length

increases; the bend testing supported this assumption. The work presented here focuses on the effects of the panel pre-wrinkling, which is one of the shortcomings of this work. Once the top skin of the panel wrinkles the cross-section loses a lot of its bending stiffness and the estimation of the panel deflection becomes more complicated. The pressure-volume work that Davids et al (2008) developed includes the effects of pressure-volume change in bending and shear to model post-wrinkling response. The research could be adapted from cylindrical airbeams to drop-stitch panels. Another shortcoming of this research is the neglect of how the drop-stitch yarns could affect the stiffness of the panel.

Chapter 5

CONCLUSIONS AND RECOMENDATIONS FOR FUTURE WORK

5.1 Summary and Conclusions

Inflatable beams, arches and panels have become increasingly popular for load-bearing applications and have a variety of military and civil applications. The popularity of these structures comes from being lightweight, easy to transport, and being able to regain shape after the structure has been overloaded and the load is removed. The majority of inflatable beams and arches – commonly termed “airbeams” – are cylindrical pressure vessels with a circular cross-section. In contrast, drop-stitch panels incorporate yarns that connect the top and bottom surfaces, giving a wide, shallow cross-section with parallel top and bottom surfaces. Unlike airbeams, drop-stich panels do not incorporate a bladder due to the presence of drop-yarns. Therefore, the majority of drop-stich panels use a coated fabric.

The primary objective of this research was to develop testing procedures to determine the constitutive properties of orthotropic neoprene/nylon drop-stitch inflatable panel fabric, and to quantify panel bending load-deflection response. This was done through panel inflation and skin coupon testing, large-scale torsion tests, and full-scale four-point bend tests. Panel inflation and skin coupon testing was done to determine the effective panel orthotropic constitutive properties in the longitudinal/warp and transverse/weft directions of the panel. Torsion testing was performed to determine the membrane shear modulus.

Traditionally, coupon level testing is utilized to determine the Poisson's ratio as well as the Young's Modulus, *E*. From the coupon testing, the average longitudinal/warp membrane modulus E_x^* was found to be 1843 lb/in. This form of testing only applies uniaxial stresses on the specimens, while inflation testing creates biaxial stresses. With different properties of the material in the longitudinal/warp and the transverse/weft directions, applying biaxial stresses to determine the membrane moduli is more accurate. Table 5.1 shows the average membrane moduli presented in Chapter 3 from inflation testing at 5, 10 and 15 psi.

Table 5.1: Average Membrane Moduli

	Long./Warp Membrane Modulus, E_x^* (lb/in)	**Tran./Weft Membrane Modulus, E_z^* (lb/in)**
5 psi	2514	2538
10 psi	2634	2654
15 psi	3394	3614

To compare the two methods of determining the membrane modulus, the coupon membrane modulus of 1843 lb/in is compared to the longitudinal/warp membrane modulus determined for 15 psi. The biaxial stress produces a more realistic modulus and is approximately 106% larger than the modulus computed from coupon-level testing. This large difference emphasizes the importance of accurately capturing biaxial stress states when estimating skin moduli. Therefore, the results from the coupon level testing are only used to determine the Poisson's ratio, $\nu_{xz} = 0.29$.

The torsion testing provided the membrane shear modulus G^*. At 5 psi, the average membrane shear modulus was $G^* = 147\ lb/in$, at 10 psi was $G^* = 181\ lb/in$ and at 15 psi was $G^* = 203\ lb/in$. The membrane shear modulus at 15 psi is almost 40% larger than the membrane shear modulus at 5 psi. As observed in the inflation testing when

determining the membrane moduli, E_x^* and E_z^*, drop-stitch inflatable panel membrane shear modulus also increases with inflation pressure. The moduli computed from the second and third cycles of testing at each pressure differ by at most 2% at the highest inflation pressure of 15 psi, and differences are even lower at 5 psi and 10 psi. While both the membrane moduli and the membrane shear modulus are pressure-dependent, there is a larger increase in membrane modulus with inflation pressure than the membrane shear modulus.

The bend tests showed a high dependence of panel stiffness and capacity on inflation pressure. For example, the 7 ft span carried a load of approximately 800 lb at a displacement of 10 inches compared with a load of about 350 lb at the same displacement when the inflation pressure was 5 psi. This corresponds to an increase in panel capacity of 129% at a displacement of 10 inches. Coupled with the increase in panel shear modulus with increasing inflation pressure, and the established increase of panel shear stiffness with inflation pressure due to pressure-volume work (Davids 2007, 2008, 2009), this result highlights the importance of maximizing in-service inflation pressure to optimize panel performance.

For the bend tests, predictions were made for the estimated deflection at the mid-span and load heads using both Euler-Bernoulli beam theory and Timoshenko beam theory with pressure-volume work. These theories predicted a stiffer response than what was actually observed in the experimental data. Euler-Bernoulli and Timoshenko beam theory both predict deflections in a beam but with two different assumptions. Euler-Bernoulli assumes that the plane sections remain plane and normal to the longitudinal axis, while in Timoshenko beam theory the plane sections do remain plane but are no longer normal to the longitudinal axis. Therefore the Euler-Bernoulli only consider the deflections due to

bending, while the Timoshenko beam includes the deflections due to shear. While both theories predicted a stiffer response than the experimental data, the Timoshenko beam theory with pressure-volume work, established by Davids et al (2008), predicts a closer response than Euler-Bernoulli beam theory. This shows that the shear deflections of the panel cannot be ignored and are just as significant to the modeling of the panel as the deflections due to bending.

5.2 Recommendations for Future Work

At present, the experimental data and constitutive properties determined in this study are being used to develop a beam-based, finite-element modeling strategy tailored to drop-stitch panels. These models will build on the methods developed by Davids (2007), Davids et al. (2008) and Davids et al. (2009), utilizing the material properties G^* and E_x^* that were experimentally determined in this phase of the research as well as fundamental physics including tension-only fabric response, pressure-volume work, and the effect of the drop-stitch yarns.

While current work is incorporating the experimental data and constitutive properties determined in this study, future work should still be done to learn more about drop-stitch panels.

- Examine the time-dependent stress-strain response of the skin material.
- Include a more accurate estimation of the panel cross-section as an idealized cross-section of two half-circles and a rectangle are not completely accurate.
- Additional 3D modeling that explicitly incorporates the drop-stitch yarns.

- While the testing done to determine the constitutive properties were suitable for initial estimates, there was a lot learned about the panels and additional tests should be done as well.
- To determine more accurate membrane moduli, cruciform tests would be beneficial. These tests can apply biaxial stress to coupons similar to the inflation testing. However, unlike the inflation testing which results in stress that is proportional to pressure in both directions, a cruciform test can introduce a constant stress in the transverse/weft direction that corresponds to a given inflation pressure, and then vary the stress seen in the longitudinal/warp direction to account for stresses caused by pressure and external loads. This method can produce a more accurate result for the membrane moduli as well as determining Poisson's ratio.
- Additionally, future research should consider using tension and torsion tests of inflated panels to produce accurate pre-tension of the panel skin due to inflation similar to those conducted by Turner et al. (2008) and Kabche et al. (2011).

REFERENCES

ASTM International. *D3039/D3039M-17 Standard Test Method for Tensile Properties of Polymer Matrix Composite Materials.* West Conshohocken, PA; ASTM International, 2017 https://doi-orf.wv-o-ursus-proxy02.ursus.maine.edu/10.1520/D3039_D3039M-17

Apedo, K.L., Ronel, S., Jacquelin, E., Massenzio, M. and Bennani, A., (2009).“Theoretical analysis of inflatable beams made from orthotropic fabric,” *Thin-Walled Structures, Elsevier*, 47(12) pp.1507-1522. https://doi.org/10.1016/j.tws.2009.06.003

Apedo, K.L., Ronel, S., Jacquelin, E., Bennani,A., and Massenzio M., (2010). “Nonlinear finite element analysis of inflatable beams made from orthotropic woven fabric,” *International Journal of Solids and Structures, Elsevier*, 47(16) pp.2017-2033. https://doi.org/10.1016/j.ijsolstr.2010.02.030

Bagnell, Daniel G., (2011). ‘Recent Advancements in the Development of Inflatable Multi-Hull Boats Utilizing Drop-Stitch Fabric’ *11th International Conference on Fast Sea Transportation FAST 2011*, Honolulu, Hawaii, USA, September.

BASF Corporation. (2003). Mehcanical Performance of Polyamides with Influence of Moisture and Temperature - Accurate Evaluation and Better Understanding. Mount Olive, New Jersey. Retrieved from http://www2.basf.us/PLASTICSWEB/displayanyfile?id=0901a5e180004880

Brayley, Kevin E., (2011). "Structural Behavior of Externally Reinforced Inflated Fabric Arches and Beams" *Electronic Theses and Dissertations*. 1568. https://digitalcommons.library.umaine.edu/etd/1568

Brayley, Kevin E., Davids, William G., and Clapp, Joshua D., (2012). “Bending response of externally reinforced, inflated, braided fabric arches and beams,” *Construction and Building Materials, Elsevier* 30 pp.50-58 doi: 10.1016/j.conbuildmat.2011.12.042

Cavallaro, Paul V., Johnson, Matthew E., Sadegh, (2003) “Mechanics of plain-woven fabrics for inflated structures,” *Composite Structures, Elselvier*, 61(4), September, pp. 375-393 https://doi.org/10.1016/S0263-8223(03)000054-0

Cavallaro, Paul V., (2006). “Technology & Mechanics Overview of Air-Inflated Fabric Structures” (Report 11,784) *Yearbook of Science & Technology, McGraw-Hill*, New York, NY.

Cavallaro, Paul V., Sadegh,Ali M., Quigley, Claudia J., (2006). "Bending Behavior of Plain-Woven Fabric Air Beams: Fluid-Structure Interaction," (IMCE2006-16307) *Proceedings of ASME International Mechanical Engineering Congress and Exposition*, Chicago, Illinois, USA. 5-10 November.

Cavallaro, Paul V., Hart, Christopher J., Sadegh, Ali M., (2013). "Mechanics of Air-Inflated Drop-Stitch Fabric Panels Subjected to Bending Loads" (NUWC-NPT Technical Report 12,141) *Naval Undersea Warfare Center Division*, Newport, Rhode Island.

Cavallaro, Paul V., Smith, Russell W.. (2015). "Conceptual Inflatable Fabric Structures for Protective Crew Quarters Systems in Space Vehicles and Space Habitat Structures," (NUWC-NPT Technical Report 12,179) *Naval Undersea Warfare Center Division*, Newport, Rhode Island.

Clapp, J.D., Davids, W.G., Goupee, A.J., and Young, A.C., (2015). "Experimental Determination of Inflatable, Braided Tube Constitutive Properties," *Strain* 52, pp.148-161 doi: 10.1111/str.12175

Davids, William G., (2007). Finite-element analysis of pressurized fabric tubes including pressure effects and local fabric wrinkling. *Finite Elements in Analysis and Design*, 44: 24-33.

Davids, William G., Zhang, Hui, (2008). "Beam finite element for nonlinear analysis of pressurized fabric beam-columns," *Engineering Structures, Elsevier* 30(7) pp.1969-1980 https://doi.org/10.1016/j.engstruct.2007.12.020

Davids, William G., (2009). "In-Plane Load-Deflection Behavior and Buckling of Pressurized Fabric Arches," *Journal of Structural Engineering*, 135(11). ISSN 04..6112/2009/11-1320-1329 https://doi-org.wv-o-ursus-proxy02.ursus.maine.edu/10.1061/(ASCE)ST.1943-541X.0000068

DiGiovanna, Lia, (2013). "Characterizing the Mechanical Properties of Drop Stitch Inflatable Structures" *Massachusetts Institute of Technology* https://hdl.handle.net/1721.1/83708

Elsabbagh, Adel, (2015). "Nonlinear finite element model for the analysis of axisymmetric inflatable beams," *Thin-Walled Structures, Elsevier* 96 pp.307-313. http://dx.doi.org/10.1016/j.tws.2015.08.021

Falls, Jaye, and Water, Jennifer K., (2011). "Bending Tests of inflatable Dropstitch Panels," *Proceedings of the 11th International Conference of Fast Sea Transportation FAST 2011*, Honolulu, Hawaii, USA, September 26-29

Felicissimo, Robert, (2015). "Exploration of the Mechanical Properties of both Ridged and Inflated Drop Stitch Fabric Material," *City University of New York (CUNY)* 688 https://academicworks.cuny.edu/cc_etds_theses/688

Gere JM and Timoshenko SP (1984). *Mechanics of Materials (2nd Ed)*. PWS Engineering, Boston MA, USA.

Kabche, Jean Paul, Peterson, Michael L., and Davids, William G., (2011). "Effect of inflation pressure on the constitutive response of coated woven fabrics used in airbeams," *Composites: Part B, Elsevier* 42 pp.526-537 https://doi.org/10.1016/j.compositesb.2010.11.007

Nguyen, Thanh-Truong, Ronel, S., Massenzio, M., Apedo, K.L., and Jacquelin, E., (2011). "Analytical buckling analysis of an inflatable beam made of orthotropic technical textiles," *Thin-Walled Structures, Elsevier* 51 pp.186-200 doi: 10.1016/j.tws.2011.10.017

Nguyen, Quang-Tung, Thomas, Jean-Christophe, and Le van, Anh, (2014). "Inflation and Bending of an orthotropic inflatable beam," *Thin-Walled Structures, Elsevier* 88 pp.129-144 http://dx.doi.org/10.1016/j.tws.2014.11.015

Puls, G. L. (1947). The Effect of Moisture on Mylon Yarns and Fabrics. *Journal of the Textile Institute Proceedings, 38*(1), 30-40.

Turner AM, Kabche JP, Peterson ML and Davids WG (2008). Tension/torsion testing of inflatable fabric tubes. *Experimental Techniques*, 32(2): 47-52.

V. Miri, O. P.-M. (2009). Effect of water absorption on the plastic deformation behavior of nylon 6. *European Polymer Journal, 45*, 757-762.

Wielgosz, Christian, Leflaive, Etienne, Dubé, Jean-François, (1998). "Experimental study and numerical modeling of inflated fabric panels," *WIT Transactions on Engineering Sciences*, 21. hal-01786681 https://hal.archives-ouvertes.fr/hal-01786681

Wielgosz, Christian, Thomas, Jean-Christophe., (2002). "Deflections of inflatable fabric panels at high pressure," *Thin-Walled Structures, Elsevier*, 40 (6), pp.523-536. https://hal.archives-ouvertes.fr/hal-01006721

Young, Andrew C., Davids, William G., Whitney, Daniel J., Clapp, Joshua D., and Goupee, Andrew J., (2017). "Structural testing and analysis of a braided, inflatable fabric torus structure," *Acta Astronautica, Elsevier* 139 pp.189-200 http://dx.doi.org/10.1016.j.sctaastro.2017.07.004

BIOGRAPHY OF AUTHOR

Elisabeth Waugh was born in Portland, Maine on September 20, 1996 to W. Scot and Patricia Waugh. She was raised in Casco, Maine on a farm that has been in the family for three generations. She attended school in SAD 61, finishing at Lake Region High School in 2014. Lake Region was where Elisabeth stayed involved in many different extracurricular activates including music, sports, theater, and student government.

Once she graduated high school, a presidential scholarship and the unknown of what to major in brought Elisabeth north to the University of Maine in Orono. Eventually she found her footing in Mechanical Engineering and has not looked back since. With great professors like Senthil Vel, Elisabeth discovered her interest in structural mechanics and composites. From there she landed a position as an undergraduate research assistant at the Advanced Structures and Composites Center, where she was then extended an offer to a graduate research assistantship. All of this has led her to where she is today and hopes to obtain a promising entry-level engineering job. Elisabeth is a candidate for the Master of Science degree in Mechanical Engineering from the University of Maine in August, 2021